



# Micropolar regularization of crystal plasticity with the gradient-enhanced incremental hardening law

M. Ryś, S. Stupkiewicz, H. Petryk\*

*Institute of Fundamental Technological Research, Polish Academy of Sciences, Pawińskiego 5B, 02-106 Warsaw, Poland*

## ARTICLE INFO

### Keywords:

Gradient plasticity  
Crystal plasticity  
Cosserat continuum  
Length scale  
Indentation size effect  
3D model

## ABSTRACT

A new model of gradient crystal plasticity is developed in which the incompatibility of plastic deformation field is simultaneously included in two different ways. The first one is well known and incorporates the gradient effect of accumulated rotation of the crystallographic lattice on the kinematic hardening in the Cosserat crystal plasticity model. The second way incorporates the effect of the current incompatibility of lattice spin on the total dislocation density rate, resulting in an additional isotropic hardening term in the gradient-enhanced hardening law. The latter effect involves a natural length scale that is fully determined in terms of standard quantities of a non-gradient hardening law and evolves during plastic deformation. The relative significance of the two effects depends on the values of material parameters, which is demonstrated by the results of calculations of 1D and 3D examples for a Cu single crystal. If the second effect is predominant, then the Cosserat formulation provides only a regularization, and then the model can be used to predict size effects. This is shown by 3D simulations of the size effect in spherical indentation of a copper single crystal. Since the gradient-enhanced hardening law does not involve any adjustable parameter, the obtained agreement of the model prediction with the experimental indentation size effect on hardness can be regarded as surprisingly good.

## 1. Introduction

It is now commonly agreed that incompatibility of plastic (or equivalently elastic) deformation, typically associated with the notion of geometrically necessary dislocations (GNDs), is one of the main mechanisms responsible for size effects in plasticity (Nye, 1953; Ashby, 1970). Here, two points of view can be adopted. The first one is that the respective size effects are governed by the incompatibility of the *accumulated* plastic deformation that can be described, for instance, by the dislocation density tensor (Nye, 1953). This approach constitutes the basis of numerous theories and models of gradient plasticity and gradient crystal plasticity (e.g., Steinmann, 1996; Gurtin, 2000; Menzel and Steinmann, 2000; Evers et al., 2004; Bayley et al., 2007; Gurtin et al., 2007; Gurtin, 2008; Kuroda and Tvergaard, 2008; Bargmann et al., 2014; Kaiser and Menzel, 2019; Jebahi et al., 2020), just to mention a few. In these approaches, a back stress appears which is expressed in terms of a quantity characterizing incompatibility of accumulated plastic deformation. This class of models includes also the Cosserat crystal plasticity model (e.g., Kröner, 1963; Forest et al., 1997; Neff et al., 2007; Forest, 2008; Cordero et al., 2010; Mayeur et al., 2011) used in this paper. The accumulated incompatibility is also the main governing factor in the so-called mechanism-based strain gradient plasticity (Nix and Gao, 1998; Gao et al., 1999) and crystal plasticity (Han et al., 2005), where the total GND density is considered as a part of the total dislocation density that is introduced into the classical Taylor formula (Taylor, 1934), thus providing a description of size effects.

\* Corresponding author.

E-mail addresses: [mrys@ippt.pan.pl](mailto:mrys@ippt.pan.pl) (M. Ryś), [stupkie@ippt.pan.pl](mailto:stupkie@ippt.pan.pl) (S. Stupkiewicz), [hpetryk@ippt.pan.pl](mailto:hpetryk@ippt.pan.pl) (H. Petryk).

According to the second point of view, not only the accumulated incompatibility of plastic deformation in a representative volume element but also a history of the underlying *incremental* plastic incompatibility needs to be taken into account. Dislocations form in general a complex three-dimensional network. Its part quantified by Nye's tensor can be reduced to a special set of *straight* GNDs whose geometric properties are not cancelled by other dislocations in the crystal (Arsenlis and Parks, 1999). In the classical dislocation-based plasticity (Kocks and Mecking, 2003), generation or annihilation of dislocations takes place at every deformation step in a statistical manner and affects the crystal hardening. However, additional GND segments can be geometrically induced by the *incremental* incompatibility of plastic flow, regardless of whether the accumulated incompatibility of plastic deformation is increased or decreased thereby. For instance, the generation of a GND segment that is dipolar to the existing one is an additional source of increasing the total dislocation length accompanied by diminishing the accumulated plastic incompatibility in the volume element. The related effect of the rate of Nye's dislocation density tensor on the rate of the *scalar* total dislocation density is missing in the first viewpoint above.

The second point of view has been adopted by Petryk and Stupkiewicz (2016) when deriving the 'minimal' gradient enhancement of conventional crystal plasticity to include size effects through a modified hardening law. In this approach, two sources of the total dislocation density *rate* are considered, namely the average density rate of statistically generated dislocations and the average density rate of dislocations induced by slip-rate gradients, and both are introduced to the Taylor formula taken also in the rate form. This seemingly small difference with respect to the approach of Nix and Gao (1998), where a similar procedure is applied but in terms of the total dislocation density rather than in the rate form, leads to a substantial difference in the final result. In particular, the gradient-enhanced hardening law derived by Petryk and Stupkiewicz (2016) involves another internal length scale which evolves during plastic deformation and is closely related to the dislocation mean free path, and thus has a clear physical interpretation. The concept of an evolving length scale has been recently employed also by Dahlberg and Boåsen (2019) and Scherer et al. (2019) in their strain gradient plasticity models.

Importantly, the natural internal length scale derived by Petryk and Stupkiewicz (2016) is expressed in terms of standard quantities of a non-gradient hardening law, so no fitting is needed (nor possible). The model is thus capable of delivering *predictions* of the corresponding size effects. Interestingly, a good prediction of the indentation size effect in spherical indentation has been obtained just by introducing the mentioned gradient-enhanced hardening law into the conventional theory of crystal plasticity (Stupkiewicz and Petryk, 2016).

It may be noted that there exists also a class of gradient crystal plasticity models that do not directly account for incompatibility of plastic deformation. This class includes, for instance, models in which gradient effects are introduced through the gradient of a scalar quantity representing the accumulated plastic slip (Wulfinghoff and Böhlke, 2012; Scherer et al., 2020).

The main idea of this work is to combine in a novel manner—within the framework of small-strain micropolar (Cosserat) plasticity—the effects associated with the two points of view discussed above. Specifically, a constitutive description of crystal plasticity is developed that includes the effects of (i) the gradient of the *accumulated* lattice rotation and (ii) the local incompatibility of plastic deformation *rate*. The first effect manifests itself through the presence of the Cosserat couple stresses and of the related back stresses in the slip-system yield conditions. The second effect manifests itself through the dependence of the rate of critical resolved shear stresses on the current rate of the dislocation density tensor and leads to the hardening law enhanced by slip-rate gradients.

The relative importance of the two effects is examined in detail in this work through illustrative examples, including 3D simulations of spherical indentation. In particular, it is shown that if the effect (ii) is predominant then the Cosserat formulation provides a regularization that is needed in the original model of Petryk and Stupkiewicz (2016). In fact, the original model admits spatial jumps in slip-rate gradients (Stupkiewicz and Petryk, 2016), which may lead to spurious oscillations in a finite-element solution (Lewandowski and Stupkiewicz, 2018). Otherwise, the combined model proposed in this work extends the Cosserat models of crystal plasticity (Forest et al., 1997; Forest, 2008) with the missing effect of additional *isotropic* hardening due to geometrically induced dislocations.

While the proposed model has not been used before, to the authors' knowledge, the general idea to combine the two effects discussed above is not entirely new. The gradient-enhanced hardening law of Petryk and Stupkiewicz (2016) has been combined with a Gurtin-type model by Ryś and Petryk (2018) and with a microcurl model by Ryś et al. (2020). The incompatibility of the accumulated plastic deformation enters the former model through the microforces conjugate to slip-rate gradients (Gurtin, 2000, 2008) and the latter one through the curl of the accumulated plastic distortion (Cordero et al., 2010; Aslan et al., 2011) introduced into the model using the micromorphic approach (Forest, 2009, 2016). By resorting to higher-order continuum descriptions that employ higher-order gradients, both models provide the needed regularization of the original model of Petryk and Stupkiewicz (2016). The micromorphic model of Ryś et al. (2020) is beneficial in terms of computational efficiency since, in a general 3D problem, it involves 9 additional global unknowns (the components of the micromorphic counterpart of the plastic distortion tensor) as compared to 12 additional global unknowns in the original formulation of Stupkiewicz and Petryk (2016) (the non-local slip rates of 12 slip systems in an FCC crystal). The dual-mixed finite element formulation (cf. Ekh et al., 2007; Ryś and Petryk, 2018) would not be computationally competitive in 3D either, since it would involve spatial gradients of slip rates projected on the respective slip planes or slip systems, thus requiring a considerable number of additional global unknowns.

Concerning computational efficiency, the model proposed in this work is highly beneficial as compared to the models discussed above since the global unknowns in a general 3D case comprise three components of the displacement field and, additionally, only three components of the Cosserat micro-rotation field. There are thus 6 global unknowns rather than 12 or even 15 unknowns in the case of other models. Accordingly, upon finite-element implementation, the model is suitable for simulation of realistic 3D indentation problems and is here applied to study the indentation size effect in spherical indentation of a copper single crystal.

Note that gradient crystal-plasticity simulations of 3D indentation are scarce in the available literature (Lee and Chen, 2010; Demiral et al., 2013; Gao et al., 2015; Stupkiewicz and Petryk, 2016; Xiao et al., 2019; Cheng et al., 2021). The proposed model may provide the simplest effective tool for performing 3D simulations in gradient crystal plasticity when incorporating simultaneously the two gradient-effects (i) and (ii) discussed above. Effect (i) is responsible for kinematic hardening, and (ii) for extra isotropic hardening, and both effects vanish if the plastic flow and lattice rotation are uniform at the continuum level.

The paper is organized as follows. In Section 2, the basic equations of small-strain micropolar (Cosserat) crystal plasticity are recalled following Forest (2008) and Cordero et al. (2010). Enhancement of the anisotropic hardening law with the effects of slip-rate gradients is presented in Section 3 following Petryk and Stupkiewicz (2016). In Section 4, finite-element implementation of the model is briefly discussed and material parameters of a high purity Cu crystal are determined, including the conventional (non-gradient) hardening law. In Section 5, two one-dimensional examples are analysed to illustrate the features of the model and to validate its finite-element implementation. Finally, the main problem of spherical indentation of a Cu crystal is studied in Section 6. The predicted indentation size effect is compared to the experimental results of Kucharski and Woźniacka (2019). A parametric study is also carried out to illustrate the relative importance of the effects introduced by the incompatibility of the accumulated plastic strain (through the Cosserat model) and of its rate (through the gradient-enhanced hardening law).

## 2. Cosserat crystal plasticity at small strain

We quote below, following Forest (2008) and Cordero et al. (2010), a set of basic equations of Cosserat (micropolar) crystal plasticity in the small deformation framework. The reader is referred to the relevant literature quoted in the introduction and to references therein for a thorough description of the theory. As all this is well known, a more detailed description is omitted here. In Section 3, the model is extended to include the gradient-enhanced hardening law proposed by Petryk and Stupkiewicz (2016).

### 2.1. Cosserat elastoplasticity

In a Cosserat (micropolar) continuum, two independent kinematic fields are introduced, namely the displacement  $\mathbf{u}$  and the micro-rotation that is represented by the infinitesimal rotation vector  $\boldsymbol{\phi}$ . Two deformation measures are then introduced. The relative deformation tensor  $\mathbf{e}$  is defined as

$$\mathbf{e} = \mathbf{H} + \boldsymbol{\epsilon} \cdot \boldsymbol{\phi}, \quad \mathbf{H} = \text{grad } \mathbf{u}, \quad (1)$$

where  $\mathbf{H}$  is the displacement gradient,  $\boldsymbol{\epsilon}$  denotes the permutation tensor, the dot denotes a single contraction,  $(\boldsymbol{\epsilon} \cdot \boldsymbol{\phi})_{ij} = \epsilon_{ijk} \phi_k$  in the common index notation with the summation convention, and the curvature tensor  $\boldsymbol{\kappa}$  is defined as

$$\boldsymbol{\kappa} = \text{grad } \boldsymbol{\phi}. \quad (2)$$

The stress measures associated with  $\mathbf{e}$  and  $\boldsymbol{\kappa}$  are the (force-)stress tensor  $\boldsymbol{\sigma}$  and the couple-stress tensor  $\mathbf{m}$ , both non-symmetric in general. The stresses satisfy the equations of the balance of momentum and of the balance of moment of momentum, which in the absence of body forces read

$$\text{div } \boldsymbol{\sigma} = \mathbf{0}, \quad \text{div } \mathbf{m} + 2 \overset{\times}{\boldsymbol{\sigma}} = \mathbf{0}, \quad (3)$$

where  $\overset{\times}{\boldsymbol{\sigma}} = -\frac{1}{2} \boldsymbol{\epsilon} : \boldsymbol{\sigma}$  is the axial vector of the skew-symmetric part of the stress tensor  $\boldsymbol{\sigma}$ , and the colon denotes a double contraction. Accordingly, using the index notation, we have  $\sigma_{ij,j} = 0$ ,  $\overset{\times}{\sigma}_i = -\frac{1}{2} \epsilon_{ijk} \sigma_{jk}$  and  $m_{ij,j} - \epsilon_{ijk} \sigma_{jk} = 0$ . The boundary conditions for the prescribed traction vector  $\mathbf{t}$  and couple-stress vector  $\mathbf{M}$  are

$$\mathbf{t} = \boldsymbol{\sigma} \cdot \mathbf{n}, \quad \mathbf{M} = \mathbf{m} \cdot \mathbf{n}, \quad (4)$$

where  $\mathbf{n}$  is the outer unit normal to the considered domain.

Considering now an elastic–plastic Cosserat solid, the displacement gradient  $\mathbf{H}$  is split additively into elastic ( $\mathbf{H}^e$ ) and plastic ( $\mathbf{H}^p$ ) parts, and so is the relative deformation tensor  $\mathbf{e}$ . The micro-rotation  $\boldsymbol{\phi}$  is assumed to contribute only to the elastic deformation so that we have

$$\mathbf{H} = \mathbf{H}^e + \mathbf{H}^p, \quad \mathbf{e} = \mathbf{e}^e + \mathbf{H}^p, \quad \mathbf{e}^e = \mathbf{H}^e + \boldsymbol{\epsilon} \cdot \boldsymbol{\phi}. \quad (5)$$

The displacement gradient and its elastic and plastic parts are in general non-symmetric and can be split into respective symmetric ( $\boldsymbol{\epsilon}^\square = \mathbf{H}_{\text{sym}}^\square$ ) and skew-symmetric ( $\boldsymbol{\omega}^\square = \mathbf{H}_{\text{skw}}^\square$ ) parts, viz.

$$\mathbf{H} = \boldsymbol{\epsilon} + \boldsymbol{\omega}, \quad \mathbf{H}^e = \boldsymbol{\epsilon}^e + \boldsymbol{\omega}^e, \quad \mathbf{H}^p = \boldsymbol{\epsilon}^p + \boldsymbol{\omega}^p, \quad (6)$$

where  $\mathbf{H}_{\text{sym}} = \frac{1}{2}(\mathbf{H} + \mathbf{H}^T)$ ,  $\mathbf{H}_{\text{skw}} = \frac{1}{2}(\mathbf{H} - \mathbf{H}^T)$ , etc.

The elastic response is governed by the constitutive equations which, in order to account for elastic anisotropy characteristic for single crystals, are adopted here in the form

$$\boldsymbol{\sigma} = \mathbb{L} : \mathbf{e}_{\text{sym}}^e + 2\mu_c \mathbf{e}_{\text{skw}}^e, \quad \mathbf{m} = 2\beta \boldsymbol{\kappa}, \quad (7)$$

where  $\mathbb{L}$  is the fourth-order elastic stiffness tensor possessing the usual minor and major symmetries, and  $\mu_c$  and  $\beta$  are two additional constants of Cosserat elasticity. Note that elastic anisotropy is here introduced only into the classical part, while the Cosserat part is

assumed isotropic (and additionally assumed to satisfy special relationships,  $\alpha = 0$  and  $\beta = \gamma$ , using the common notation, cf. Forest (2008)). Parameter  $\beta$  affects an intrinsic length scale of the micropolar continuum, which depends also on the shear moduli, cf. Section 5.1.

The term involving parameter  $\mu_c$  in Eq. (7) can be interpreted as a penalty term that penalizes the difference between the elastic rotation associated with  $\omega^e$  and the Cosserat micro-rotation  $\phi$ . Indeed, for  $\sigma$  to be bounded as  $\mu_c$  increases indefinitely, we must have

$$\mathbf{e}_{\text{skw}}^c = \omega^e + \epsilon \cdot \phi \approx \mathbf{0} \quad \rightarrow \quad \overset{\times}{\omega}^e \approx \phi, \quad (8)$$

where  $\overset{\times}{\omega}^e = -\frac{1}{2} \epsilon : \omega^e$  is the axial vector of  $\omega^e$ .

## 2.2. Crystal plasticity

As usual in the crystal plasticity theory, the rate  $\dot{\mathbf{H}}^P$  of plastic distortion is assumed to be a sum of the plastic distortion rates on individual slip systems indexed by  $\alpha$ ,

$$\dot{\mathbf{H}}^P = \sum_{\alpha} \dot{\gamma}_{\alpha} \mathbf{N}_{\alpha}, \quad \mathbf{N}_{\alpha} = s_{\alpha} \otimes \mathbf{m}_{\alpha}, \quad (9)$$

where  $\dot{\gamma}_{\alpha}$  is the slip rate,  $\mathbf{m}_{\alpha}$  the slip-plane normal, and  $s_{\alpha}$  the slip direction such that  $s_{\alpha} \cdot \mathbf{m}_{\alpha} = 0$  to ensure plastic incompressibility. As usual,  $\otimes$  denotes a tensor product.

The generalized resolved shear stress  $\tau_{\alpha}$  for the slip system  $\alpha$  is defined as

$$\tau_{\alpha} = \sigma : \mathbf{N}_{\alpha} = \tau_{\alpha}^{\text{sym}} - X_{\alpha}, \quad \tau_{\alpha}^{\text{sym}} = \sigma_{\text{sym}} : (\mathbf{N}_{\alpha})_{\text{sym}}, \quad X_{\alpha} = -\sigma_{\text{skw}} : (\mathbf{N}_{\alpha})_{\text{skw}}. \quad (10)$$

The first term,  $\tau_{\alpha}^{\text{sym}}$ , is the classical resolved shear stress associated with the symmetric part of the stress tensor  $\sigma$ . The second term,  $X_{\alpha}$ , can be interpreted as a back stress. From Eq. (3)<sub>2</sub>, we have  $\sigma_{\text{skw}} = -\epsilon \cdot \overset{\times}{\sigma} = \frac{1}{2} \epsilon \cdot \text{div } \mathbf{m}$ , thus the back stress  $X_{\alpha}$  is related to the divergence of the couple stress tensor  $\mathbf{m}$ ,

$$X_{\alpha} = -\frac{1}{2} (s_{\alpha} \times \mathbf{m}_{\alpha}) \cdot \text{div } \mathbf{m}, \quad (11)$$

where  $\times$  denotes a vector product.

As in the conventional rate-independent crystal plasticity, the slip system  $\alpha$  is activated when the corresponding resolved shear stress  $\tau_{\alpha}$  reaches the threshold,  $\tau_{\alpha}^c$ . Defining the yield function  $f_{\alpha}$ ,

$$f_{\alpha} = |\tau_{\alpha}| - \tau_{\alpha}^c = |\tau_{\alpha}^{\text{sym}} - X_{\alpha}| - \tau_{\alpha}^c, \quad (12)$$

the yield condition and the plastic flow rule can be expressed as follows,

$$f_{\alpha} \leq 0, \quad (\text{sign } \tau_{\alpha}) \dot{\gamma}_{\alpha} \geq 0, \quad f_{\alpha} \dot{\gamma}_{\alpha} = 0. \quad (13)$$

In the present finite-element implementation, a viscous regularization of the plastic flow rule is employed, as discussed in Section 4.1.

To complete the model, a hardening law that governs the evolution of  $\tau_{\alpha}^c$  must be specified. This is usually done by adopting the following form,

$$\dot{\tau}_{\alpha}^c = \sum_{\alpha} h_{\alpha\beta} |\dot{\gamma}_{\beta}| = \theta \sum_{\alpha} q_{\alpha\beta} |\dot{\gamma}_{\beta}|, \quad (14)$$

where  $h_{\alpha\beta}$  are the state-dependent hardening moduli that specify self ( $\alpha = \beta$ ) and latent ( $\alpha \neq \beta$ ) hardening, and  $h_{\alpha\beta} = \theta q_{\alpha\beta}$  with  $\theta$  as an isotropic hardening modulus. In Section 3, this conventional hardening law is extended to include the effect of slip-rate gradients.

## 2.3. Dislocation density tensor

The total deformation gradient  $\mathbf{H}$  is compatible, hence its curl vanishes, thus

$$\text{curl } \mathbf{H} = \text{curl } \mathbf{H}^e + \text{curl } \mathbf{H}^P = \mathbf{0}, \quad (15)$$

while the elastic and plastic parts of  $\mathbf{H}$  are not compatible in general. The curl of a tensor is here defined such that for  $\mathbf{A} = \text{curl } \mathbf{B}$  we have  $A_{ij} = \epsilon_{jkl} B_{il,k}$  (a note of caution: other conventions using a transpose or a minus sign are also met in the literature).

The dislocation density tensor  $\alpha$  is introduced as a measure of the incompatibility of plastic deformation (Kröner, 1958, 1981; De Wit, 1981; Naghdi and Srinivasa, 1993; Steinmann, 1996; Acharya and Bassani, 2000; Menzel and Steinmann, 2000; Forest et al., 2000; Cermelli and Gurtin, 2002; Cordero et al., 2010; Mayeur et al., 2011; Yavari and Goriely, 2012),

$$\alpha = \text{curl } \mathbf{H}^P = -\text{curl } \mathbf{H}^e = -\text{curl } \epsilon^e - \text{curl } \omega^e. \quad (16)$$

Neglecting the curl of the elastic strain,  $\text{curl } \epsilon^e \approx \mathbf{0}$ , the dislocation density tensor is approximated as

$$\alpha \approx -\text{curl } \omega^e, \quad (17)$$

and this is actually the form of the dislocation density tensor that was originally derived by Nye (1953).

Lattice rotation is defined as the difference between the material rotation  $\omega$  and the plastic rotation  $\omega^p$ , hence  $\omega^e = \omega - \omega^p$  is recognized as the lattice rotation. In view of Eq. (5)<sub>3</sub>, we have

$$\omega^e = e_{\text{skw}}^e - \epsilon \cdot \phi. \quad (18)$$

The Cosserat micro-rotation  $-\epsilon \cdot \phi$  can thus be identified with the lattice rotation  $\omega^e$  when  $e_{\text{skw}}^e = \mathbf{0}$ . As discussed in Section 2.1, this condition is approximately satisfied when parameter  $\mu_c$  is sufficiently large, and then we have

$$\omega^e \approx -\epsilon \cdot \phi. \quad (19)$$

Accordingly, in view of Eq. (17), the dislocation density tensor  $\alpha$  can be approximated using the Cosserat micro-rotation (cf. Forest *et al.*, 1997; Forest, 2008), viz.

$$\alpha \approx -\text{curl} \omega^e \approx \text{curl}(\epsilon \cdot \phi). \quad (20)$$

Using the identity:  $\text{curl}(\epsilon \cdot \phi) = (\text{grad} \phi)^T - (\text{div} \phi)\mathbf{1}$ , we finally have, cf. Nye (1953),

$$\alpha \approx \kappa^T - (\text{tr} \kappa)\mathbf{1}, \quad (21)$$

so that the dislocation density tensor  $\alpha$  is approximated using the curvature tensor  $\kappa$ , which in view of Eq. (19) is identified as the lattice curvature. This expression is suitable for finite-element implementation within the Cosserat continuum framework and, in particular, can be used to effectively implement the gradient-enhanced hardening law that is discussed in the subsequent section.

### 3. Gradient-enhanced hardening law

In this section, the conventional hardening law (14) is extended to include slip-rate gradient effects. The formulation below is taken from Petryk and Stupkiewicz (2016), where a more detailed presentation and discussion can be found.

Consider first the case when the slip-rate gradients are absent or negligible. The corresponding conventional hardening law (14) can be rewritten in the following form,

$$\dot{\tau}_\alpha^c = \dot{\tau}^c + \theta \sum_\beta (q_{\alpha\beta} - 1) |\dot{\gamma}_\beta|, \quad \dot{\tau}^c = \theta \dot{\gamma}, \quad \dot{\gamma} = \sum_\alpha |\dot{\gamma}_\alpha|, \quad (22)$$

where  $\tau^c$  is the isotropic flow stress and  $\dot{\gamma}$  is the effective slip rate. Note that the second term in Eq. (22)<sub>1</sub> vanishes when  $q_{\alpha\beta} = 1$ , i.e., when latent and self hardening are equal, which justifies the interpretation of  $\tau^c$  as the isotropic flow stress. The hardening law is often specified by postulating  $\tau^c$  as a function of the accumulated slip  $\gamma$ ,

$$\tau^c = \tau_\gamma(\gamma), \quad \dot{\tau}^c = \theta \dot{\gamma}, \quad \theta = \frac{d\tau_\gamma(\gamma)}{d\gamma}, \quad (23)$$

so that the hardening modulus  $\theta$  can be identified with the derivative of the master curve  $\tau_\gamma(\gamma)$ , cf. Eq. (22). However, the conventional hardening law Eq. (22) or Eq. (23) is no longer appropriate if  $\dot{\tau}^c$  depends on the dislocation density rate that is affected by slip-rate gradients.

The (generalized) Taylor formula (Taylor, 1934), which is one of the basic phenomenological laws in the materials science literature on plasticity of metals, provides a relationship between the flow stress  $\tau^c$  and the total dislocation density  $\rho$ ,

$$\tau^c = \tau_\rho(\rho) = a\mu b\sqrt{\rho}, \quad (24)$$

where  $\mu$  is the elastic shear modulus,  $b$  is the Burgers vector modulus, and coefficient  $a$  is a given material constant. The rate of  $\tau^c$  can thus be expressed in terms of the rate of  $\rho$ ,

$$\dot{\tau}^c = \tau'_\rho \dot{\rho}, \quad \tau'_\rho = \frac{d\tau_\rho(\rho)}{d\rho} = \frac{a\mu b}{2\sqrt{\rho}} = \frac{(a\mu b)^2}{2\tau^c}. \quad (25)$$

Now, the dislocation density rate  $\dot{\rho}$  is decomposed into the sum of the density rate  $(\dot{\rho})_S$  of statistically generated dislocations and of the density rate  $(\dot{\rho})_G$  of dislocations induced by the current slip-rate gradients,

$$\dot{\rho} = (\dot{\rho})_S + (\dot{\rho})_G. \quad (26)$$

It is stressed that the above split concerns the rates rather than the total density  $\rho$ , which means that the current dislocation sources are split according to their statistical or geometrical character. This is different from the approach by Ashby (1970), Fleck *et al.* (1994), Nix and Gao (1998) and others, in which the total dislocation density itself is split into the densities of statistically stored dislocations (SSD) and geometrically necessary dislocations (GND).

The statistical accumulation of dislocations is described by the known formula (Kocks and Mecking, 2003),

$$(\dot{\rho})_S = \frac{1}{b\lambda} \dot{\gamma} - k_r \dot{\gamma}, \quad (27)$$

where the first term describes multiplication of dislocations, with  $\lambda$  denoting the dislocation mean free path, and the second term describes annihilation of dislocations, assumed proportional to  $\dot{\gamma}$ , where the proportionality factor  $k_r$  can be related to the mean critical distance of dislocation annihilation (Essmann and Mughrabi, 1979).

Further, it is postulated that the geometrically induced dislocation rate  $(\dot{\rho})_G$  is related to the rate of the dislocation density tensor  $\alpha$  according to

$$(\dot{\rho})_G = \frac{1}{b} \dot{\chi}, \quad \dot{\chi} = \|\dot{\alpha}\|, \tag{28}$$

where  $\dot{\chi}$  is the *effective slip-rate gradient*, and  $\|\dot{\alpha}\| = \sqrt{\dot{\alpha} : \dot{\alpha}}$ . It is worth noting that in the case of cyclic deformation, the dislocation density tensor  $\alpha$  can return to zero while the time integral of  $(\dot{\rho})_G$  is always non-decreasing and contributes to isotropic hardening, in contrast to the accumulated GND density.

Substituting the dislocation density rate  $\dot{\rho}$ , Eqs. (26)–(28), in Eq. (25)<sub>1</sub>, the rate of the isotropic flow stress can be expressed in the following form,

$$\dot{\tau}^c = \underbrace{\frac{(1 - k_r b \lambda) \tau'_\rho}{b \lambda}}_{\theta} \left( \dot{\gamma} + \underbrace{\frac{\lambda}{1 - k_r b \lambda}}_{\ell} \dot{\chi} \right). \tag{29}$$

For  $\dot{\chi} = 0$ , the above expression reduces to Eq. (23)<sub>2</sub> with the term in the front identified as the hardening modulus  $\theta$ , and, secondly, the term in front of  $\dot{\chi}$ , denoted by  $\ell$ , has the dimension of length, thus

$$\theta = \frac{(1 - k_r b \lambda) \tau'_\rho}{b \lambda}, \quad \ell = \frac{\lambda}{1 - k_r b \lambda} = \frac{\tau'_\rho}{b \theta}, \tag{30}$$

given that  $\theta \neq 0$ . Note that Eq. (30)<sub>1</sub> provides a relationship between the hardening modulus  $\theta$ , defined by Eq. (23), and the generalized Taylor formula in Eq. (24)<sub>1</sub>.

If the classical Taylor formula (24)<sub>2</sub> is adopted as the specification of the function  $\tau_\rho$ , the isotropic hardening rule (29) can be written in its final form,

$$\dot{\tau}^c = \theta(\dot{\gamma} + \ell \dot{\chi}), \quad \ell = \frac{a^2 \mu^2 b}{2 \tau^c \theta}. \tag{31}$$

By substituting Eq. (31) in the conventional anisotropic hardening law (22)<sub>1</sub>, the following gradient-enhanced anisotropic hardening law is obtained (Petryk and Stupkiewicz, 2016),

$$\dot{\tau}_\alpha^c = \theta \sum_{\beta} q_{\alpha\beta} |\dot{\gamma}_\beta| + \underbrace{\theta \ell \dot{\chi}}_{\text{PS term}}, \quad \theta \ell = \frac{a^2 \mu^2 b}{2 \tau^c}, \tag{32}$$

in which a particularly simple form of the slip-rate gradient effect is described by the term that will be referred to as the ‘PS term’, while the first term in Eq. (32)<sub>1</sub> remains intact with respect to the conventional anisotropic hardening law (14). The coefficient  $\theta \ell$  at  $\dot{\chi}$  and the internal length scale  $\ell$  are expressed, in an explicit form, solely in terms of standard quantities of a non-gradient hardening law, hence no additional assumptions are needed. Moreover, it follows from Eq. (30)<sub>2</sub> that the internal length scale  $\ell$  has a physical interpretation through its relation to the dislocation mean free path  $\lambda$ , and reduces simply to  $\ell = \lambda$  for  $k_r = 0$ , i.e., in the absence of dislocation annihilation. It also follows that the internal length scale  $\ell$  is not a constant parameter, as usually assumed in various gradient plasticity theories, but evolves during the deformation process as a function of the current values of  $\tau^c$  and  $\theta$ . In view of the minimal set of physically-based assumptions, Eqs. (24)–(28), and the important properties discussed above, the gradient enhancement of the classical theory of crystal plasticity solely by the extended incremental hardening law, Eq. (32), has been termed ‘minimal’ by Petryk and Stupkiewicz (2016).

When the dislocation density tensor  $\alpha$  is specified in the form (21) as in Nye (1953) then the effective slip-rate gradient takes the form

$$\dot{\chi} = \sqrt{\dot{\kappa} : \dot{\kappa} + (\text{tr } \dot{\kappa})^2} \approx \|\text{curl } \omega^e\|, \tag{33}$$

which by formula (28) is proportional to the density rate  $(\dot{\rho})_G$  of dislocations induced by the current slip-rate gradients. This is the essence of the proposed combination of the gradient-enhanced hardening law (32) with the Cosserat crystal plasticity theory outlined in Section 2. Eq. (33)<sub>1</sub> provides an explicit equation for the effective slip-rate gradient  $\dot{\chi}$  expressed solely in terms of the lattice spin gradient  $\dot{\kappa}$  that is introduced to the PS term for the first time in the present work.

## 4. Preliminaries to computations

### 4.1. Finite element implementation

In order to illustrate the ability of the model to capture size effects, the balance equations (3) in the respective weak forms have been implemented in a displacement-based finite-element code. The computational scheme requires that the components of the micro-rotation are introduced as global degrees of freedom in addition to the standard displacement unknowns. The resulting global set of the coupled finite-element equations is solved monolithically by the Newton method. On the local level, the implicit backward-Euler integration scheme has been employed to obtain incremental constitutive equations that are solved by using the Newton scheme. More details are provided in Appendix.

The implementation has been done with the use of the *AceGen* code generator, which combines the symbolic capabilities of *Mathematica* and an automatic differentiation (AD) technique, and together with the *AceFEM* module provides a convenient system for generating numerical procedures and computing particular problems (Korelc, 2009; Korelc and Wriggers, 2016).

In the computations presented in the next sections we consider 1D shear tests and a 3D spherical indentation problem. In the case of 1D examples, there are only two global degrees of freedom per node (one displacement and one micro-rotation). Both displacement and micro-rotation fields are interpolated using linear shape functions and one Gauss point per element is used for numerical quadrature. In each case, the 1D domain is discretized into 1000 elements. Such a fine discretization is needed to accurately represent the steep gradient of the micro-rotation in the shearing problem studied in Section 5.1.

In the 3D spherical indentation problem, the global unknowns comprise three standard displacements and three micro-rotations, which results in six degrees of freedom in each node. This is an advantage with respect to the computational models used previously where, in 3D problems, 15 degrees of freedom were needed in the model of Stupkiewicz and Petryk (2016) and 12 degrees of freedom would be needed in the micromorphic model proposed by Rys et al. (2020). Importantly, the number of additional degrees of freedom is independent here on how many slip systems are considered. A hexahedral eight-node element is used in which both the displacements and the micro-rotations are interpolated with trilinear shape functions. In order to avoid volumetric locking effects, the element formulation is based on the Taylor expansion of shape-function derivatives, a technique similar to that used by Korelc et al. (2010).

In the indentation problem, the indenter is modelled as a rigid sphere, and the contact problem is assumed to be frictionless. The augmented Lagrangian method combined with the nodal integration is used to enforce the impenetrability constraints on the contact surface (Alart and Curnier, 1991; Lengiewicz et al., 2011). Furthermore, the couple-stress vector  $\mathbf{M}$ , cf. Eq. (4)<sub>2</sub>, is assumed to vanish on the entire free surface, thus also in the actual contact zone. Accordingly, no additional non-standard contact conditions are imposed, even if the Cosserat model admits such conditions (Lewandowski-Szewczyk and Stupkiewicz, 2020).

The rate-independent constitutive model described in Section 2.2 suffers from the well-known problem of non-uniqueness in the selection of active slip systems. In this paper, this difficulty refers only to the 3D example, where the full set of 12 slip systems is considered. To circumvent this difficulty in a frequently used way, the rate-independent flow rule (12) has been replaced by its rate-dependent version which yields the following expression for the plastic slip rate on each slip system as a function of the corresponding resolved shear stress (Hutchinson, 1976),

$$\dot{\gamma}_\alpha = \dot{\gamma}_0 \operatorname{sign}(\tau_\alpha) \left( \frac{|\tau_\alpha|}{\tau_\alpha^c} \right)^m. \quad (34)$$

This modification introduces two additional parameters, the reference slip rate,  $\dot{\gamma}_0$ , and the exponent  $m$  which characterizes rate sensitivity. In order to ensure that the response is possibly close to the rate-independent one, according to the quasi-static behaviour of metals like Cu at room temperature, these parameters are set to  $\dot{\gamma}_0 = 0.001 \text{ s}^{-1}$  and  $m = 50$ .

#### 4.2. Setting the materials parameters

Since the ultimate aim of this article is to demonstrate the ability of the model developed in Sections 2 and 3 to predict the indentation size effect quantitatively, careful selection of the material parameters is needed. This is done for a high purity Cu crystal whose response in the spherical indentation (Kucharski and Woźniacka, 2019) is taken for verification purposes.

Standard elastic constants  $c_{11} = 170 \text{ GPa}$ ,  $c_{12} = 124 \text{ GPa}$ ,  $c_{44} = 75 \text{ GPa}$  for a Cu cubic crystal are taken after Schmid and Boas (1950), Simmons and Wang (1971).

The conventional anisotropic part in the gradient-enhanced hardening law (32) is taken in the frequently adopted form,  $q_{\alpha\beta} = \chi_{\alpha\beta} + q(1 - \chi_{\alpha\beta})$ , with  $\chi_{\alpha\beta} = 1$  for coplanar slip systems and zero otherwise. A latent hardening parameter  $q = 1.4$  is taken after Kocks (1970). The following formula for isotropic hardening modulus  $\theta$  is adopted after Bronkhorst et al. (1992),

$$\theta = \theta_0 \left( 1 - \frac{\tau^c}{\tau_{\max}} \right)^p \quad \text{for } \tau_0 \leq \tau^c \leq \tau_{\max}, \quad \theta = 0 \quad \text{otherwise.} \quad (35)$$

It is intended to describe stages III and IV of strain hardening, omitting Stage I of easy glide which may be absent in the confined plastic flow under the indenter. The parameters in formula (35) are selected as follows. The exponent  $p = 2$  is taken for a better qualitative description of Stage IV than Voce's  $p = 1$  (cf. Kocks and Mecking, 2003, Figs. 20,21). Parameters  $\theta_0 = 250 \text{ MPa}$  and  $\tau_{\max} = 120 \text{ MPa}$  have been identified from the [001] uniaxial compression curve with no gradient effect (S. Kucharski, private communication) of a high-purity Cu single crystal examined by Kucharski and Woźniacka (2019). These values are dependent on the latent hardening parameter  $q$  and on the number of simultaneously active slip systems in the high-symmetry direction [001], taken equal to 4 (two of them coplanar) to fulfil the boundary constraints under compression.

The only parameter that has been identified from the indentation test itself was the initial yield shear stress  $\tau_0$ . For pure copper,  $\tau_0 \approx 1 \text{ MPa}$  would roughly correspond to the beginning of Stage I strain hardening (cf. Schmid and Boas, 1950; Kocks and Mecking, 2003, Fig. 1). However, significance of the easy glide stage in the case of confined plastic flow in the spherical indentation test is debatable, and this stage is absent in formula (35). Therefore, for the remaining material parameters as above, the parameter  $\tau_0 = 6 \text{ MPa}$  has been adopted to adjust the level of the indentation load to the level observed in the experiment performed by Kucharski and Woźniacka (2019) for only one, the largest value  $R = 250 \text{ }\mu\text{m}$  of the indenter radius.

Parameters  $a$ ,  $\mu$  and  $b$  that enter through the Taylor formula (24) into the gradient-enhanced part of the hardening law (32) represent the last group of material parameters to be specified. Following Sauzay and Kubin (2011) as a representative source from the materials science literature, we adopt as in Petryk and Stupkiewicz (2016) the strengthening coefficient  $a = 0.33$  for Cu, and the

**Table 1**  
Material parameters for a Cu single crystal used in numerical simulations.

$c_{11}$ [GPa]	$c_{12}$ [GPa]	$c_{44}$ [GPa]	$\tau_0$ [MPa]	$\theta_0$ [MPa]	$\tau_{\max}$ [MPa]	$p$ [-]	$q$ [-]	$\dot{\gamma}_0$ [s <sup>-1</sup> ]	$m$ [-]	$a$ [-]	$\mu$ [GPa]	$b$ [nm]	$\mu_c$ [GPa]	$\beta$ [GPa $\mu\text{m}^2$ ]
170	124	75	6	250	120	2	1.4	0.001 <sup>a</sup>	50 <sup>a</sup>	0.33	40.3	0.256	403 <sup>b</sup>	0.0025 <sup>c</sup>

<sup>a</sup>This parameter is only used in 3D examples.

<sup>b</sup>In 1D examples,  $\mu_c = 1000$  GPa is used.

<sup>c</sup>In 1D examples,  $\beta$  is treated as a case-study parameter.

shear modulus  $\mu$  as the one for  $\langle 110 \rangle \{ 111 \}$  slip systems, i.e.  $\mu = (c_{11} - c_{12} + c_{44})/3 = 40.3$  GPa. Finally, the Burgers vector modulus is  $b = 0.256$  nm for Cu, which completes the specification of parameters of the hardening law (32).

In the Cosserat model, there are two further parameters  $\mu_c$  and  $\beta$  that also need to be specified. The first parameter,  $\mu_c$ , is treated throughout this paper as a penalty parameter which must be high enough so that the micro-rotation field  $\phi$  be close to the lattice rotation  $\phi^c$ . From a computational point of view, however, the value of  $\mu_c$  cannot be arbitrarily high. In this paper, the value of the penalty parameter is chosen to be  $\mu_c = 1000$  GPa in 1D examples and  $\mu_c = 10\mu$  in 3D examples. In both cases, the value of  $\mu_c$  is sufficiently high to make the rotation of crystallographic lattice close enough to the Cosserat rotation. Moreover,  $\mu_c = 1000$  GPa adopted in 1D examples leads to numerical results almost identical to analytical ones for  $\mu_c \rightarrow \infty$ .

Estimating the value of the second parameter,  $\beta$ , is more demanding, especially if it is considered as a real physical parameter. There are few works (e.g., Kröner, 1963; Sedláček and Forest, 2000; Forest and Sedláček, 2003) where, in the case of simple examples, the authors proposed an expression for calculating  $\beta$  based on its physical interpretation. However, in most other works the parameter is usually represented as  $\beta = l_e^2 \mu$ , where  $l_e$  is an elastic length scale, and is treated as a case study parameter (e.g., Mayeur et al., 2011; Cordero et al., 2010), or a fitting parameter in the cases where the model is aimed to reproduce results comparable to discrete dislocation dynamics (DDD) simulations (e.g., Mayeur and McDowell, 2011, 2015; Chang et al., 2012) or experimental results (e.g., Forest et al., 2000). In this work, the Cosserat model is treated primarily as a convenient and efficient regularization approach to encompass the PS term effectively, hence parameter  $\beta$  is left unspecified for case study.

The material parameters used in numerical simulations are summarized in Table 1.

## 5. Numerical and analytical 1D examples

First, we will examine two one-dimensional (1D) examples analysed in the literature. In the first example, see Fig. 1a, simple shear of a two-phase laminate is considered following Forest and Sedláček (2003) and Cordero et al. (2010). This example is a nice illustration of the performance of the Cosserat crystal plasticity model in describing dislocation pile-up effects at phase boundaries. In the case of no hardening, the corresponding 1D problem can be solved analytically (Forest and Sedláček, 2003; Cordero et al., 2010). In this work, the example is extended to include strain hardening and its gradient enhancement proposed by Petryk and Stupkiewicz (2016) and described in Section 3. The aim here is to examine the slip-rate gradient effects introduced by the PS term, see Eq. (32). The analytical solution for the non-hardening case is also used to validate the finite-element implementation of the Cosserat crystal plasticity model.

The second example concerns shearing of a constrained strip with two symmetric slip systems, see Fig. 1b. This problem has been studied in numerous works (e.g. Shu et al., 2001; Bittencourt et al., 2003; Evers et al., 2004; Yefimov and Van der Giessen, 2005; Bayley et al., 2006). Here we refer to the semi-analytical solution obtained by Stupkiewicz and Petryk (2016), which exhibits a sharp kink in the middle of the strip due to the gradient enhancement of the hardening law adopted after Petryk and Stupkiewicz

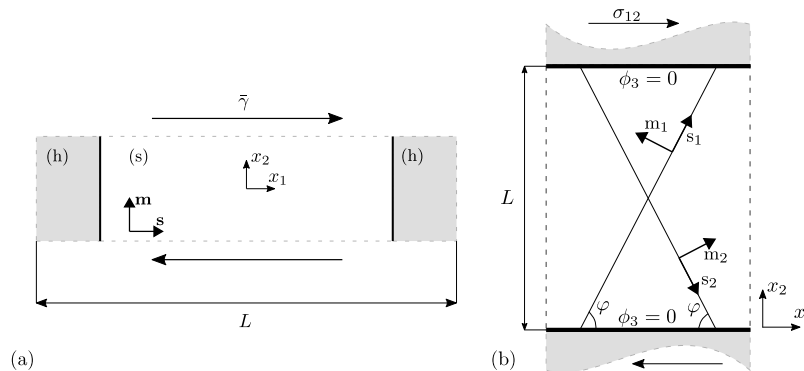


**Fig. 1.** Schematic of the shearing problem: (a) shearing of a periodic single-slip single crystal composed of soft (s) and hard (h) phases, and (b) shearing of a double-slip single crystal.

(2016). The aim of this example is to illustrate that the Cosserat model is capable of regularizing the kink while capturing the essential features of the solution.

Isotropic elasticity is assumed throughout this section with the elastic shear modulus  $\mu = 40.3$  GPa. The remaining material parameters are as specified in Section 4.2, unless stated otherwise.

### 5.1. Shearing of a two phase periodic microstructure: single slip case

In the first example we consider a periodic microstructure composed of two phases, the elastoplastic soft phase in the middle and the purely elastic hard phase on both sides (denoted by subscripts 's' and 'h', respectively), see Fig. 1a. The soft phase is an elastoplastic Cosserat continuum with a single slip system of the slip-plane normal aligned with the  $x_2$  axis. The hard phase is an elastic Cosserat continuum that acts as a barrier for dislocation movement. The two-phase microstructure is subjected to a uniform shear strain  $\bar{\gamma}$  in the  $x_1$  direction, which results in a plastic shear  $\gamma(x_1)$  in the soft phase. It is assumed further that the soft and hard phases have a different  $\beta$  modulus,  $\beta_s \neq \beta_h$ , whereas  $\mu_c$  is the same for both phases.

Following Forest and Sedláček (2003), we consider displacement and micro-rotation fields of the form:

$$u_1 = \bar{\gamma}x_2, \quad u_2 = u_2(x_1), \quad u_3 = 0, \quad \phi_1 = \phi_2 = 0, \quad \phi_3 = \phi_3(x_1), \quad (36)$$

with unknown displacement  $u_2(x_1)$  and micro-rotation  $\phi_3(x_1)$ . Periodic boundary conditions are imposed on  $u_2(x_1)$  and  $\phi_3(x_1)$  and both fields are continuous at phase boundaries.

For the problem defined above, there are two non-zero components of the Cosserat deformation,  $e_{12} = \bar{\gamma} + \phi_3$  and  $e_{21} = u_{2,1} - \phi_3$ , and one non-zero component of the curvature tensor,  $\kappa_{31} = \phi_{3,1}$ . Consequently, there are two non-zero components of the stress tensor,  $\sigma_{12}$  and  $\sigma_{21}$ , and one non-zero component of the couple-stress tensor,  $m_{31} = 2\beta\kappa_{31}$ .

The assumption of single slip implies that  $e_{12} = e_{12}^e + \gamma$  and  $e_{21} = e_{21}^e$ , where  $\gamma = 0$  in the hard phase, so that the balance equations yield

$$\begin{aligned} \sigma_{21,1} &= \mu(u_{2,11} - \gamma_{,1}) + \mu_c(\gamma_{,1} - 2\phi_{3,1} + u_{2,11}) = 0, \\ m_{31,1} - (\sigma_{12} - \sigma_{21}) &= \beta\phi_{3,11} - \mu_c(\bar{\gamma} - \gamma + 2\phi_3 - u_{2,1}) = 0. \end{aligned} \quad (37)$$

The plastic flow criterion formulated for the resolved shear stress  $\tau = \sigma_{12}$  takes the following form

$$|\tau| = |\mu(e_{12}^e + e_{21}^e) - X| \leq \tau^c, \quad (38)$$

where the back stress  $X$  can be expressed as  $X = \beta\phi_{3,11}$ , cf. Eq. (11), and the critical resolved shear stress  $\tau^c$  is governed by the gradient-enhanced incremental hardening law (32),

$$\dot{\tau}^c = \theta|\dot{\gamma}| + \theta\ell\dot{\chi}, \quad \theta\ell = \frac{a^2\mu^2b}{2\tau^c}, \quad \dot{\chi} = \|\dot{\alpha}\| = |\dot{\phi}_{3,1}|. \quad (39)$$

Assuming no hardening,  $\theta = \theta_0 = 0$ , which implies that the PS term is also neglected, the two above balance equations can be reduced to a third-order differential equation in each phase which can be solved analytically (Forest and Sedláček, 2003; Cordero et al., 2010). Upon enforcing the continuity and periodicity conditions, the solution results in a hyperbolic and parabolic profile of  $\phi_3$  in the hard and soft phase, respectively. In the hard phase, from the solution it follows that the size-effect is related to the intrinsic length scale  $l_h = \sqrt{\beta_h(\mu + \mu_c)/(\mu\mu_c)}$  which in the case of  $\mu_c \rightarrow \infty$  tends to  $l_h = \sqrt{\beta_h/\mu}$ . The whole problem, however, is rather complex and size effects depend on many factors, e.g., on parameters  $\beta_s$  and  $\beta_h$ , and on the volume fraction of both phases. A more detailed discussion can be found in Forest and Sedláček (2003) and Cordero et al. (2010). In the case of non-zero hardening,  $\theta \neq 0$ , with or without the PS term, the solution is obtained numerically, and the finite element method is used for that purpose.

Fig. 2 shows the macroscopic stress  $\Sigma_{12}$  (average of  $\sigma_{12}$ ) at 0.01 average plastic strain, as a function of the characteristic size  $L$  of the two-phase microstructure (note the log-log scale). Three cases are considered: (i) the full model including hardening and the PS term, (ii) the model with hardening, but without the PS term, and (iii) the model with no hardening (and no PS term). The calculations have been performed for the soft phase volume fraction  $f_s = 0.7$ . The presented curves feature a typical sigmoidal shape, where the size-independent response of conventional crystal plasticity is observed for sufficiently large  $L$  and, on the other hand, for very small values of  $L$ , the macroscopic stress tends to an upper bound, the value of which here is 670 MPa. The intermediate stage is a range where size effects take place and can be characterized, for instance, by the slope of the tangent line, deflection point, etc. (Cordero et al., 2010).

In Fig. 2a, the results are reported for a constant mismatch between the moduli of the two phases,  $\beta_h = \beta_s/100$ . Here, the curves for the no-hardening case are shifted in parallel to each other towards smaller values of  $L$  with decreasing  $\beta_s$ . The results in Fig. 2b correspond to a constant modulus in the hard phase,  $\beta_h = 0.06$  GPa  $\mu\text{m}^2$ , while  $\beta_s$  is varied,  $\beta_s = \{0.06, 6\}$  GPa  $\mu\text{m}^2$ . Accordingly, with increasing  $\beta_s$  the mismatch between the moduli also increases, which leads to a different representation of the overall behaviour than in the previous case. The finite-element results for the no-hardening case are compared to the analytical ones, and a perfect correspondence is obtained.

Including the hardening increases the lower limit of the response, while the other characteristics of the curves are the same as in the no-hardening case. Including the PS term, however, results in a further increase in the macroscopic stress in an intermediate range of values of  $L$ . The increase is more significant for smaller values of  $\beta_s$ .

In Fig. 3, the micro-rotation and plastic strain profiles are shown at 0.05 average plastic strain for  $L = 10$   $\mu\text{m}$  ( $f_s = 0.7$ ). Simulations have been performed for  $\beta_h = 0.06$  GPa  $\mu\text{m}^2$  and for two values of  $\beta_s = \{0.06, 6\}$  GPa  $\mu\text{m}^2$ . It is recalled that the micro-rotation is continuous, and the apparent jump at the interface, visible in Fig. 3a for  $\beta_s = 6$  GPa  $\mu\text{m}^2$ , represents in fact a steep

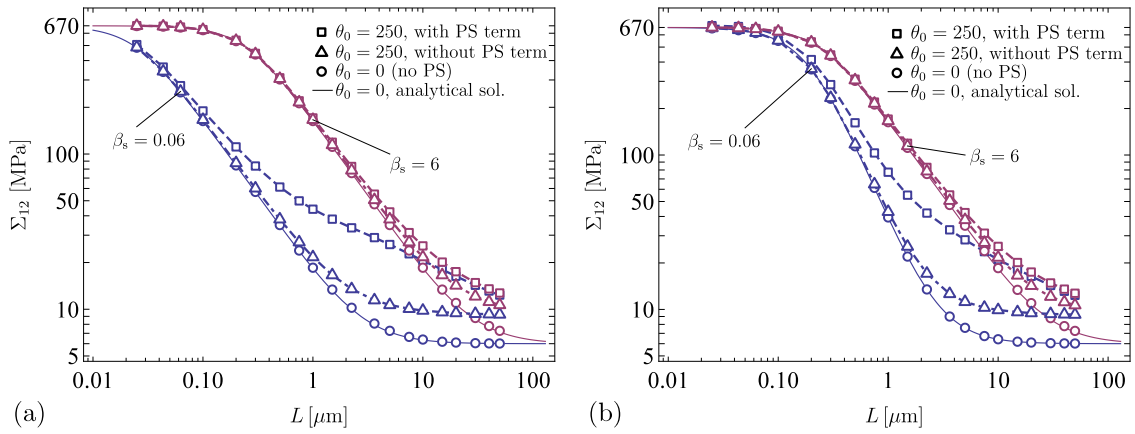


Fig. 2. Macroscopic stress  $\Sigma_{12}$  at 0.01 average plastic strain as a function of the microstructure length  $L$  for (a) the same mismatch between moduli  $\beta_h = \beta_s/100$  and  $\beta_s = \{0.06, 6\}$  GPa  $\mu\text{m}^2$ , and (b) for increasing mismatch between moduli, i.e.,  $\beta_h = 0.06$  GPa  $\mu\text{m}^2$  and  $\beta_s = \{0.06, 6\}$  GPa  $\mu\text{m}^2$ .

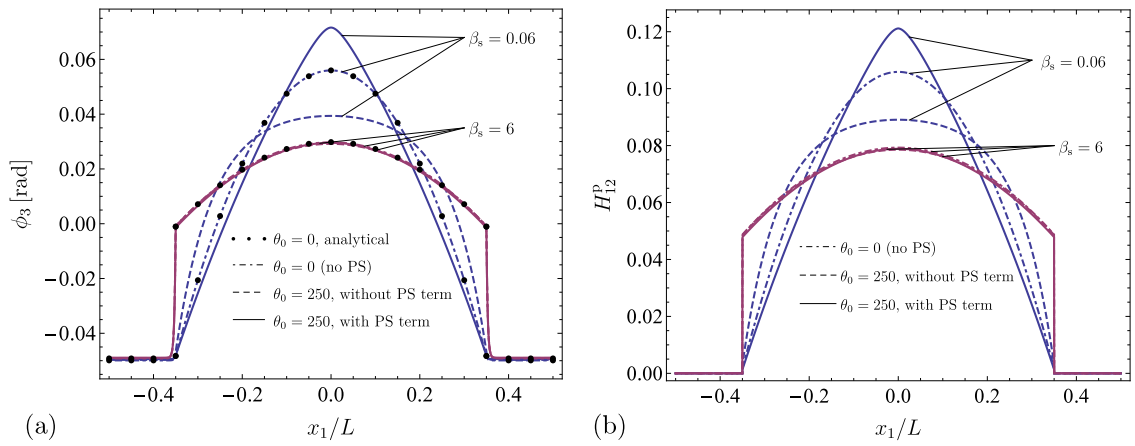


Fig. 3. Profiles of (a) the micro-rotation  $\phi_s$  and (b) plastic deformation  $H_{12}^p$  at 0.05 average plastic strain computed for the same  $\beta_h = 0.06$  GPa  $\mu\text{m}^2$  modulus and various  $\beta_s = \{0.06, 6\}$  GPa  $\mu\text{m}^2$  modulus ( $L = 10 \mu\text{m}$ ,  $f_s = 0.7$ ).

gradient of the microrotation within the hard phase. The plastic strain is discontinuous at the interface (being equal to zero in the hard phase), while the jump magnitude depends on the model parameters. In the no-hardening case, the finite-element results (dots) are compared to the analytical ones (solid lines) and again a perfect agreement is obtained. Including hardening as well as the PS term changes the profile significantly, which is seen in the case of  $\beta_s = 0.06$  GPa  $\mu\text{m}^2$ . For smaller values of parameter  $\beta_s$ , both the micro-rotation and the plastic strain are highly non-uniform within the soft phase, while for larger values of  $\beta_s$  the profiles become flat in the soft phase.

In Fig. 4a, the macroscopic stress at 0.01 average plastic strain is shown as a function of parameter  $\beta_s$  (while  $\beta_h = \beta_s/100$ ) for three microstructural lengths  $L$ . For a constant ratio  $\beta_s/\beta_h$ , the response of the Cosserat model (no hardening, no PS term) exhibits sigmoidal curves that are shifted horizontally for different  $L$ , analogically as in Fig. 2a. Importantly, if  $\beta_h \rightarrow 0$ , the analytical solution predicts no size effects regardless of the value of  $\beta_s$ . As it can be seen, the importance of the PS term is affected by both  $L$  and modulus  $\beta_s$ . The upper limit is not changed by the PS term since its effect is negligible for high values of  $\beta_s$  contrary to the lower limit which is changed significantly.

The relative size of the soft and hard phases is also a key parameter. In general, if the volume fraction of the hard phases tends to zero ( $f_s \rightarrow 1$ ), the conventional response is retrieved. Similarly, if  $\beta_h \rightarrow 0$ , the model is also incapable of predicting the size effects. In both situations, this is related to inability of transmitting the surface couples from the soft to the hard phase (Forest and Sedláček, 2003). In Fig. 4b, the macroscopic stress at 0.01 average plastic strain is shown as a function of parameter  $\beta_s$  (while  $\beta_h = \beta_s/100$ ) for three volume fractions  $f_s$  of the soft phase. It can be seen that the upper limit decreases when the relative size of the hard phase is getting smaller. However, when the PS term is included, then the model still keeps its ability to introduce size effects even for  $f_s$  close to unity, at least for smaller values of  $\beta_s$ . Hence, introduction of the PS term seems to be an important complement of the crystal plasticity Cosserat model, here demonstrated in the case where elastic inclusions play a major role in size-affected hardening.

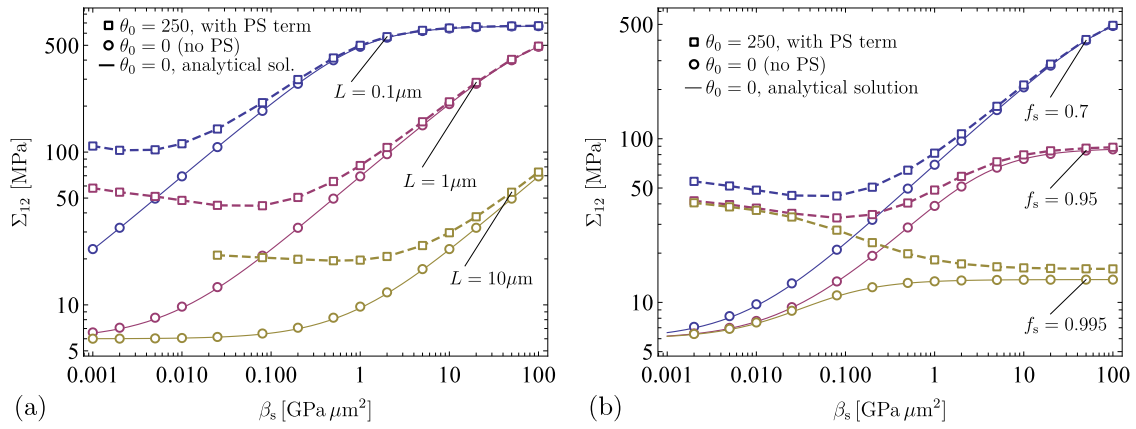


Fig. 4. Macroscopic stress  $\Sigma_{12}$  at 0.01 average plastic strain as a function of the modulus  $\beta_s$  (while  $\beta_h = \beta_s/100$ ) for (a)  $f_s = 0.7$  and three microstructure lengths  $L = \{0.1, 1, 10\} \mu\text{m}$  and (b) for  $L = 1 \mu\text{m}$  and three fractions of the soft phase.

5.2. Double slip in a constrained strip: comparison with the semi-analytical model

In this subsection, we investigate the problem of shearing of a constrained strip of thickness  $L$ , as presented in Fig. 1b. The strip with two symmetric slip systems ( $\alpha = 1, 2$ ), of the orientation specified by  $\varphi = \pi/3$ , is subjected to shearing in plane-strain conditions. Only isotropic hardening is considered here, thus  $q = 1$ , so that  $h_{\alpha\beta} = \theta$ . The symmetry implies that  $\gamma_1 = \gamma_2$  and  $\tau_1 = \tau_2$  which are both negative for  $\sigma_{12} > 0$  and  $\varphi = \pi/3$ .

A similar problem has been considered by Stupkiewicz and Petryk (2016), where a semi-analytical solution has been found for the gradient-enhanced crystal plasticity model of Petryk and Stupkiewicz (2016). In that problem, plastic slip rates are constrained at the boundaries, which corresponds to the so-called micro-clamped boundary conditions. The Cosserat model involves micro-rotations as additional degrees of freedom, thus in general it is not possible to impose a boundary condition on plastic slips, as in the original problem of Stupkiewicz and Petryk (2016). However, in this particular example, it is sufficient to restrict rotations on the boundaries to reflect the zero dislocation flux condition, at least for a relatively small value of parameter  $\beta$  (cf. Mayeur and McDowell, 2013, 2014).

We consider displacement and micro-rotation fields of the form:

$$u_1 = u_1(x_2), \quad u_2 = 0, \quad u_3 = 0, \quad \phi_1 = \phi_2 = 0, \quad \phi_3 = \phi_3(x_2), \tag{40}$$

with unknown  $u_1(x_2)$  and  $\phi_3(x_2)$  and with the boundary conditions  $u_1(0) = 0, u_1(L) = \langle H_{12} \rangle L$  and  $\phi_3(0) = \phi_3(L) = 0$ , where  $\langle H_{12} \rangle$  is a prescribed, monotonically increasing overall shear strain. For the so-defined problem, there are two non-zero components of the Cosserat deformation,  $e_{12} = u_{1,2} + \phi_3 = H_{12} + \phi_3$  and  $e_{21} = -\phi_3$ , and one non-zero component of the curvature tensor,  $\kappa_{32} = \phi_{3,2}$ . Consequently, there are two non-zero components of the stress tensor,  $\sigma_{12}$  and  $\sigma_{21}$ , and one non-zero component of the couple-stress tensor,  $m_{32} = 2\beta\kappa_{32}$ . From balance equations (3) it follows that  $\sigma_{12}$  does not depend on  $x_2$  while  $m_{32}(x_2)$  satisfies the equation  $m_{32,2} = 2\beta\phi_{3,22} = \sigma_{12} - \sigma_{21}$ . The plastic flow criterion is obtained in the following form

$$|\tau| = |\mu(e_{12}^e + e_{21}^e) \cos 2\varphi - X| \leq \tau^c, \tag{41}$$

where

$$\dot{\tau}_1^c = \dot{\tau}_2^c = \dot{\tau}^c = \theta(\dot{\gamma} + \ell \dot{\chi}), \quad \dot{\gamma} = |\dot{\gamma}_1| + |\dot{\gamma}_2|, \quad \theta\ell = \frac{a^2 \mu^2 b}{2\tau^c}, \quad \dot{\chi} = |\dot{\phi}_{3,2}|, \tag{42}$$

and the back stress  $X$  is given by  $X = -\beta\phi_{3,22}$ .

The semi-analytical solution of the original problem of Stupkiewicz and Petryk (2016) exhibits a kink in the profile of  $\gamma$ , which is due to the specific definition of the effective slip-rate gradient  $\dot{\chi}$ , here defined by the absolute value of the first derivative of the micro-rotation rate, Eq. (42)<sub>4</sub>. In the present model, the kink is regularized by including the second derivative of the micro-rotation in Eq. (41), through the back stress  $X$  with  $\beta > 0$ , the part of the model that comes from the Cosserat formulation. In the computations, the value of parameter  $\beta = 0.1 \text{ GPa } \mu\text{m}^2$  has been selected in such a way that the couple stresses  $m_{32}$  and hence the size-dependent back stress  $X$ , Eq. (10)<sub>3</sub>, does not influence the response significantly, but on the other hand,  $\beta$  is high enough to provide the required regularization. A high value of the parameter  $\mu_c = 1000 \text{ GPa}$  has been adopted.

In Fig. 5, the finite-element results obtained for the present Cosserat crystal plasticity model (dashed lines) are compared to the semi-analytical solution of the original problem of Stupkiewicz and Petryk (2016) (solid lines). The overall response in terms of the uniform normalized shear stress,  $\bar{\sigma}_{12} = \sigma_{12}/\sigma_{12}^0$  (with  $\sigma_{12}^0 = |\cos 2\varphi|\tau_0$ ) versus the overall shear strain is plotted in Fig. 5a. In Fig. 5b, the shear strain profiles,  $H_{12}(x_2)$ , at the overall shear strain  $\langle H_{12} \rangle = 0.05$  are shown for different values of strip thickness  $L$ . It can be seen in Fig. 5b that the kink in the  $H_{12}$  profiles, characteristic for the problem considered by Stupkiewicz and Petryk (2016), is properly smoothed by the Cosserat model. At the same time, the essential features of the solution, including the size effects, are properly captured by the Cosserat crystal plasticity model enhanced by the PS term.

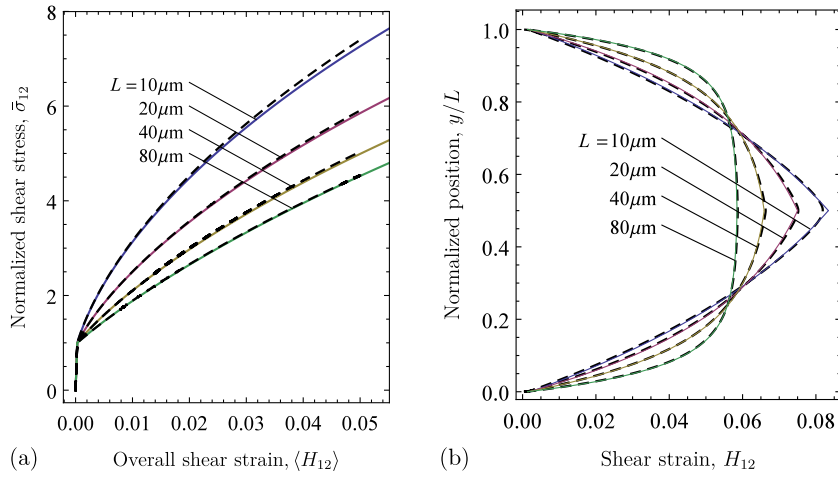


Fig. 5. Comparison of the semi-analytical solution of Stupkiewicz and Petyk (2016) (solid lines) with the present FE solution for  $\beta = 0.1\text{GPa}\mu\text{m}^2$  and  $\mu_c = 1000\text{GPa}$  (broken lines): (a) overall stress–strain response, (b) shear strain profiles for overall shear strain  $\langle H_{12} \rangle = 0.05$ .

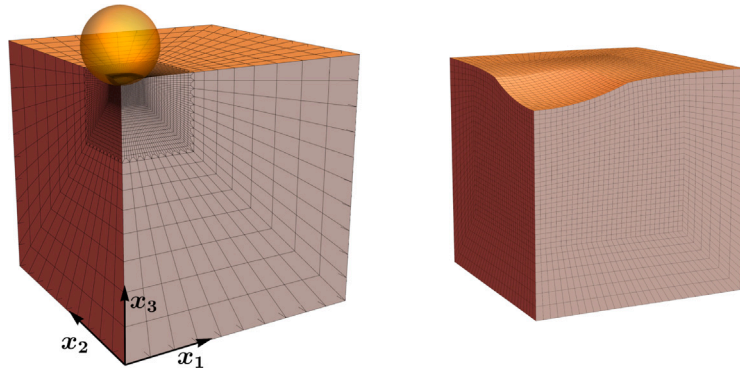


Fig. 6. Finite element mesh of the computational domain (left) and an enlarged detail of the mesh showing the deformation pattern beneath the indenter (right).

## 6. 3D Indentation size effect

### 6.1. Spherical indentation: size effect in comparison with experiment

As the main example, we present numerical simulations of the spherical indentation in a (001)-oriented fcc single crystal of high-purity copper for several radii of the indenter. The finite element mesh used in the example is shown in Fig. 6. The computational domain has been reduced to one quarter due to crystal symmetry, therefore additional constraints have been applied on the  $x_1x_3$  and  $x_2x_3$  planes. On the  $x_1x_3$  plane the normal displacement and the  $\phi_1$  and  $\phi_3$  micro-rotations are blocked whereas on the  $x_2x_3$  plane the normal displacement and the  $\phi_2$  and  $\phi_3$  micro-rotations are blocked. The computational domain (a cube) has been divided into three regions of different mesh density in order to reduce the number of unknowns and save computational time. The edge of the cube is  $16.8a_{\text{max}}$  long where  $a_{\text{max}} = \sqrt{h_{\text{max}}(2R - h_{\text{max}})}$  denotes the nominal contact radius related to the maximum penetration depth  $h_{\text{max}}$ . The edge of the square zone in which contact conditions are checked is taken as  $1.4a_{\text{max}}$  and discretized with a finer regular mesh, i.e., the edge of the length of  $1.4a_{\text{max}}$  is discretized with 30 elements. The total number of degrees of freedom is about 500,000 which makes the computational task quite demanding. All calculations have been performed for a constant ratio of the maximum penetration depth  $h_{\text{max}}$  to the indenter radius  $R$ , i.e.,  $h_{\text{max}}/R = 0.12$ , and the maximum penetration depth  $h_{\text{max}}$  has been achieved at a constant velocity  $v = h_{\text{max}}/t_{\text{max}}$  in  $t_{\text{max}} = 100\text{s}$ . Note that the normalized velocity  $v/R$  is thus constant for all radii.

The standard material parameters of high purity copper used in the 3D simulations are as specified in Section 4.2. Regarding additional parameters, we took here  $\mu_c = 10\mu = 403\text{GPa}$  which was found sufficient to meet the requirements mentioned in Section 4.2, in particular, the components of the tensor  $e_{\text{skw}}^c$  are of the order of  $10^{-8}$ , hence  $\phi \approx \omega^c$  as desired, and the contribution of the penalty term to the total elastic strain energy is below 3%. It is worth mentioning that although the stress tensor,  $\sigma$ , is non-symmetric locally, symmetry is achieved in an average sense, i.e.,  $\langle \sigma_{ij} \rangle \approx \langle \sigma_{ji} \rangle$ .

As has been shown in the previous section, the effect of the PS term is highly influenced by parameter  $\beta$  and, in particular, for high values of  $\beta$ , the PS term may have a negligible influence on the response. In the present section, for the purposes of experimental

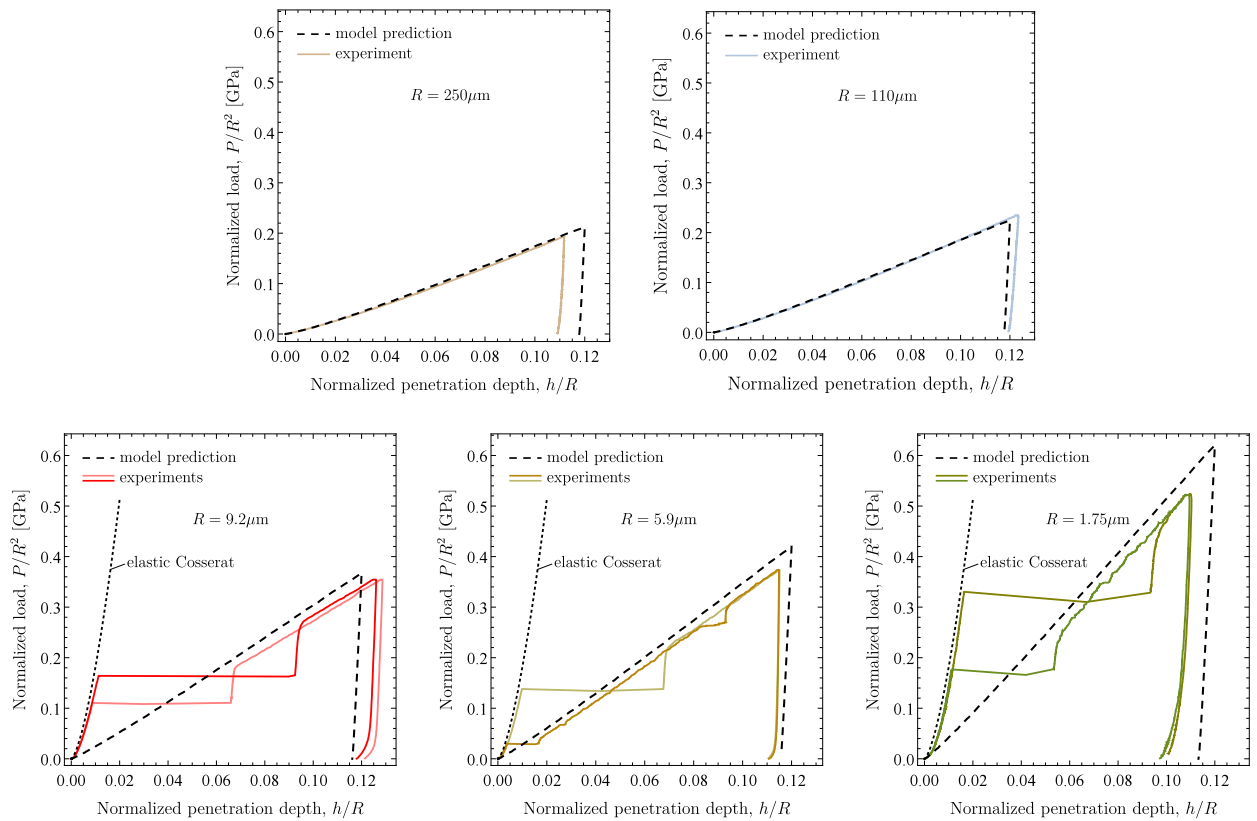


Fig. 7. Spherical indentation of a (001)-oriented Cu single crystal: normalized size-dependent load–penetration curves corresponding to different indenter radii, as indicated in the individual diagrams. Experimental results are taken from Kucharski and Woźniacka (2019).

validation of the model predictions, the parameters of the Cosserat part of the model are not treated as material parameters of physical meaning for Cu but rather as numerical regularization parameters. Hence,  $\beta$  is taken small enough not to distort the effect of the PS term, but not too small because of the required regularization. In the computations reported here,  $\beta = 0.0025 \text{ GPa}\mu\text{m}^2$  has been assumed so that the curvature term of the Cosserat model does not influence the macroscopic response significantly (cf. Section 6.2, Fig. 13).

The model has been validated versus the experimental data reported by Kucharski and Woźniacka (2019). Those authors performed spherical indentation tests on a (001)-oriented, high-purity (99.9999 pct) Cu single crystal for several tip radii,  $R = \{1.75, 5.9, 9.2, 110, 250\} \mu\text{m}$ , and for various maximum penetration depths. The tests were performed a number of times for each radius, and very good repeatability of the results was obtained, which is well illustrated in Fig. 5a of the reference for  $R = 5.9 \mu\text{m}$ . For each radius, representative diagrams of the normalized load ( $P/R^2$ ) vs. the normalized penetration depth ( $h/R$ ), taken from the reference, are shown in Fig. 7. For the smaller indenter radii, the well known pop-in events (horizontal jumps at different load levels) are visible in the figures, which are random in nature and are characterized by an unstable behaviour.<sup>1</sup> Importantly, after the pop-in events the load–penetration curves, for a specific radius, follow almost the same path in the elastic–plastic regime. It can therefore be concluded that the basic elastic–plastic part of the response after the pop-in is not influenced by pop-in events (Kucharski and Woźniacka, 2019). This enables comparison with the present simulations where the pop-in events are not modelled.

Fig. 7 compares the results of the computations carried out using the Cosserat crystal plasticity model with the PS term (dashed lines) to the experimental results discussed above. The purely elastic Cosserat response (dotted lines) is also included in the diagrams as a reference for the experimental response prior to pop-in. It can be seen that, for smaller indenter radii, the model slightly overestimates the macroscopic response (after a pop-in, if present). Nevertheless, the agreement with the experimental data is highly satisfactory in view of *no* internal length scale adjusted to obtain that agreement. It is emphasized again that the results for all indenter radii have been obtained for the same set of parameters, all but one determined independently of the indentation tests, as described in Section 4.2.

<sup>1</sup> In the literature (e.g., Shim et al., 2008), such pop-in events are attributed to a low initial density of dislocations and to the lack of dislocation sources in a volume affected by contact stresses so that the response is initially elastic. The pop-in is then caused by a sudden activation of existing dislocations or nucleation of new dislocations, which is a process of a discrete and random nature that cannot be described by a deterministic continuum model.

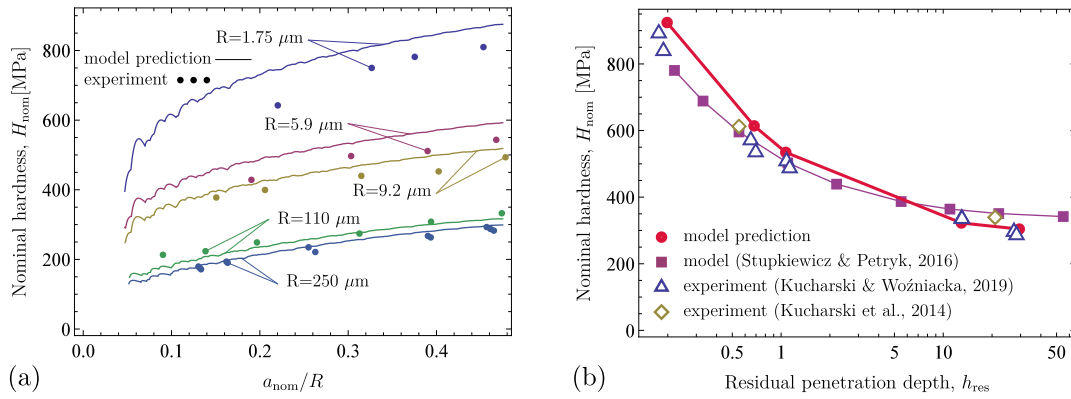


Fig. 8. Size effect in spherical indentation: (a) dependence of the nominal hardness on the normalized nominal contact radius; (b) dependence of the nominal hardness on the residual penetration depth for the ratio  $h_{res}/R \approx 0.11$ .

In Fig. 8, the indentation size effect predicted by the model is characterized in terms of the nominal hardness and is compared to the experimental results taken from Kucharski and Woźniacka (2019). All the experimental points were determined based on the respective residual indentation depths ( $h_{res}$ ), i.e.,  $H_{nom} = P/A_{nom}$ , where  $A_{nom} = \pi a_{nom}^2$ , and  $a_{nom} = \sqrt{h_{res}(2R - h_{res})}$  is the nominal contact radius.

The experimental nominal hardness  $H_{nom}$  as a function of the normalized contact radius,  $a_{nom}/R$ , is shown in Fig. 8a for various tip radii. The model predictions in this figure are calculated in terms of the current penetration depth, rather than for the residual one. Thus, since  $h_{res}$  is somewhat less than  $h_{max}$ , the actual difference between the model and the experiment is slightly bigger than that apparent in Fig. 8a. Nevertheless, the overall agreement is satisfactory. The model results are depicted by the solid lines whose irregularities are due to the successive nodes of the finite-element mesh entering into contact with the indenter.

The dependence of the nominal hardness on the residual penetration depth is shown in Fig. 8b. The predictions of the present model are compared to the experimental results of Kucharski and Woźniacka (2019), both corresponding to  $h_{res}/R \approx 0.11 \pm 0.01$ . Fig. 8 shows also the experimental data of Kucharski et al. (2014) obtained for a Cu single crystal of the orientation C1 that is close to the (001) orientation. The results are also compared to the previous model predictions obtained by Stupkiewicz and Petryk (2016) using a different regularization, finite deformation setting, somewhat different hardening parameters and corresponding to a fixed ratio  $h_{max}/R = 0.11$ . In the absence of any fitting of the length-scale parameter, the visible agreement of the predicted and experimental size-effect on nominal hardness can be regarded as highly satisfactory. This validates the theoretical approach based on the ‘minimal’ gradient extension of the conventional crystal plasticity proposed by Petryk and Stupkiewicz (2016) as a predictive tool to describe the size effect, at least on nominal hardness in the spherical indentation test.

In addition to the size-dependent hardness and force–penetration depth diagrams, the experiments exhibit size effects also in terms of the geometry of the residual imprints (Kucharski and Woźniacka, 2019). The residual imprints predicted by the model are also influenced by the indenter radius, as shown in Fig. 9, but the experimentally observed size effects are not fully captured by the model, in particular, in quantitative terms. The predicted imprints feature typical anisotropic topography with pile-up and sink-in regions, in a qualitative agreement with the experiment. The predicted heights of the pile-ups tend to be smaller with decreasing radii, which is also in a qualitative agreement with the experiment. The summits, however, are too high and too sharp in comparison with the experimental observations. As demonstrated by Petryk et al. (2017), the calculated surface topography after indentation depends significantly on the details of the hardening curve, such as its curvature and initial yield stress. The accuracy of the description of these details is limited by adoption of the simple formula (35), possibly also by other assumptions in the model, which makes it difficult for the present model to describe the surface topography adequately. Moreover, in the experiment, the sink-ins decrease in magnitude with decreasing indenter radius so that the shape of the contact area gradually changes from quadratic to circular as the indenter radius decreases (Kucharski and Woźniacka, 2019). Both effects are not captured by the model in its present form.

Fig. 10 shows the distributions of the accumulated plastic slip,  $\gamma$ , in the vicinity of the indenter in the unloaded state. For larger radii ( $R = 250$  and  $110 \mu\text{m}$ ), the plastic deformation accumulates right under the indenter, whereas for smaller radii the maximum values of  $\gamma$  appear at some distance from the surface and have a specific ‘V’ shape. The maximum value of the accumulated plastic slip,  $\gamma_{max}$ , decreases with decreasing the indenter radius.

The GND density distributions, defined as the norm of Nye’s tensor,  $\|\alpha\|$ , are presented in Fig. 11. As expected, the maximum value of the GND density increases with decreasing radius. The distribution is directly related through Eq. (21) to the lattice curvature which is accommodated by the GNDs. It is accompanied by the additional increase of the scalar total density of dislocations related to the PS term, cf. Eq. (26), which is not included in  $\alpha$ .

Fig. 12 shows the distributions of the components of the Cosserat micro-rotation which, as discussed in Section 2.3, corresponds to the lattice rotation (for a sufficiently high parameter  $\mu_c$ , which is the case here). The micro-rotation field exhibits a weak size dependence thus the maps are shown only for the biggest,  $R = 250 \mu\text{m}$ , and the smallest,  $R = 1.75 \mu\text{m}$ , radius. The micro-rotation

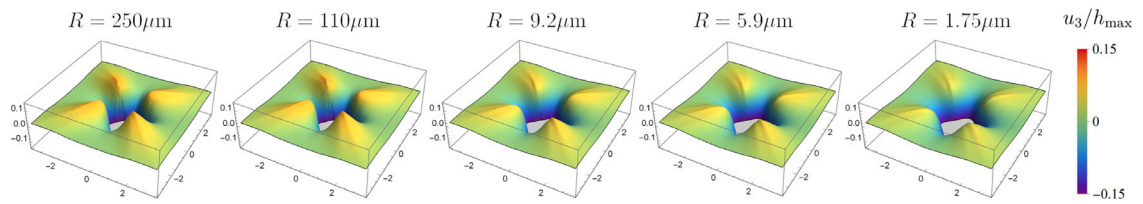


Fig. 9. Size-dependent normalized residual impressions. The normal displacement  $u_3$  is normalized by the maximum depth  $h_{\max}$ , the in-plane position is normalized by the nominal radius  $a_{\text{nom}} = \sqrt{h_{\max}(2R - h_{\max})}$ .

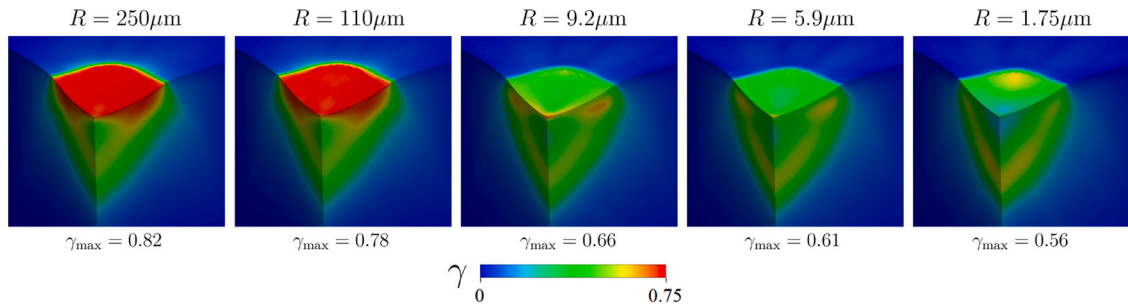


Fig. 10. Distributions of the accumulated slip  $\gamma$  shown in the unloaded state in the vicinity of the indenter for various tip radii.

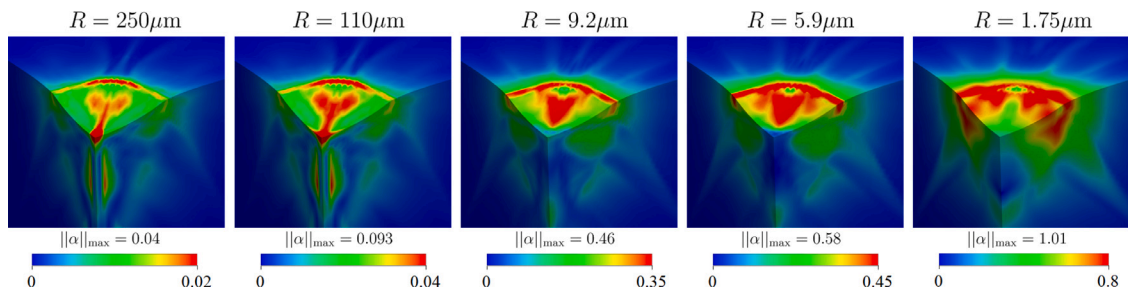


Fig. 11. The norm of Nye's tensor,  $\|\alpha\|$  in  $1/\mu\text{m}$ , as the measure of GND distribution (unloaded state).

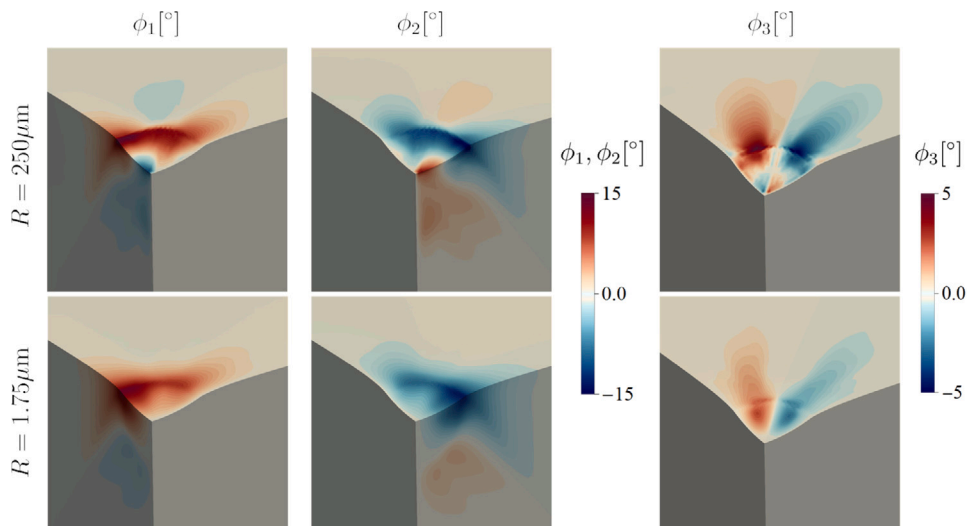


Fig. 12. Distributions of the components of the micro-rotation field for  $R = 250 \mu\text{m}$  (top) and  $R = 1.75 \mu\text{m}$  (bottom).

field exhibits a characteristic symmetry related to the crystal symmetry with respect to the  $x_1 = x_2$  plane, namely  $\phi_2$  is a mirror image of  $\phi_1$  with a minus sign, and  $\phi_3$  is antisymmetric. It is also seen that the micro-rotations are more localized and the maximum values are larger for the larger indenter.

## 6.2. Insufficiency of the Cosserat model without the PS term

As it has been shown in the previous examples, the PS term may have or not a crucial impact on the size-affected response. For example, in Fig. 4 in Section 5.1 it is clearly seen that, in the case of the two-phase microstructure, for small  $\beta$  the PS term has a crucial impact but for large  $\beta$  the PS term seems to be redundant. A natural question arises whether the satisfactory prediction of the indentation size effect on hardness through the PS term, given in Section 6.1, can be simulated by the Cosserat model without this term if the value of  $\beta$  is appropriately adjusted. The answer is negative, as shown below.

Fig. 13 presents the calculated nominal hardness,  $H_{\text{nom}}$ , versus parameter  $\beta$  in the case of 3D spherical indentation for  $R = 1.75 \mu\text{m}$  and for a fixed ratio  $h_{\text{max}}/R = 0.12$ . The results are compared to the experimental data for  $h_{\text{res}}/R \approx 0.11 \pm 0.01$  as above. The computations have been performed for a slightly coarser mesh than in the previous section, i.e., for 300,000 unknowns instead of 500,000, in order to reduce the computation time. Two cases are considered, one where the full model is employed and the other one where the PS term is disregarded (the classical Cosserat pure crystal plasticity model). The computations have been performed for various values of  $\beta$  varied between 0.00005 and  $250 \text{ GPa } \mu\text{m}^2$ . Note the similarity of the diagrams in Fig. 13 to those in Fig. 4b for  $f_s = 0.995$ .

When the PS term is disregarded (square markers), we have obtained the sigmoidal shape expected from Fig. 4, where for small values of  $\beta$  the response is very close to the conventional, size-independent crystal plasticity, whereas for larger  $\beta$  an upper limit is reached. Note that for the value used in Section 6.1 ( $\beta = 0.0025 \text{ GPa } \mu\text{m}^2$ ) the response is very close to the conventional plasticity, which proves that the size effects obtained in the previous section are solely due to the PS term. However, the highest values obtained for the Cosserat model without the PS term (for high  $\beta$ ) are much beneath the experimental value which suggest that the classical Cosserat model alone is insufficient to predict the indentation size effect on hardness.

The insufficiency of the Cosserat model can be easily explained. For small values of  $\beta$ , the model predicts high GND density (Fig. 14a-c), however, the related high values of lattice curvature do not cause a significant non-local back stress, since  $\beta$  is small. On the other hand, for increasing  $\beta$ , the curvature  $\kappa$  is reduced since it is penalized by the related elastic energy, hence ultimately much lower values of the GND density  $\|\alpha\|$  are obtained (Fig. 14d), and, again, the non-local back stress does not affect the response sufficiently.

When the full model is considered (triangular markers in Fig. 13), then, contrary to the case of the pure Cosserat model, the upper limit is obtained for small values of  $\beta$ . With increasing  $\beta$ , the hardness decreases and ultimately converges to the one predicted by the model without the PS term. This is because the curvature  $\kappa$  decreases with increasing  $\beta$ , as discussed above, and so does its rate,  $\dot{\kappa} \approx \dot{\alpha}^T$ . The PS term depends on  $\dot{\alpha}$ , and thus the effect of the PS term diminishes. This situation is similar to that seen in the 1D example of Section 5.1, where increasing  $\beta$  ultimately resulted in the PS term having little impact.

Our additional studies on the Cosserat model with the PS term have revealed that the parameter  $\beta$  has also an effect on the convergence of the results with mesh refinement. Fig. 15 shows the nominal hardness as a function of the density of the finite-element mesh. The results indicate that, when the parameter  $\beta$  is decreased, a finer mesh is needed to achieve convergence. Indeed, for  $\beta = 0.005 \text{ GPa } \mu\text{m}^2$ , the convergence is (nearly) achieved for the finest mesh considered (360,000 degrees of freedom). For  $\beta = 0.0025 \text{ GPa } \mu\text{m}^2$ , the trend suggests that the hardness would slightly increase with further mesh refinement (which has not been

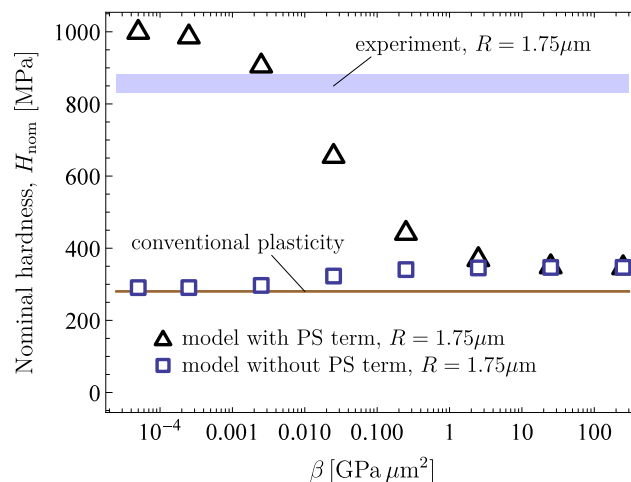


Fig. 13. Nominal hardness in the 3D indentation problem for  $R = 1.75 \mu\text{m}$  for various values of  $\beta$  varied between 0.00005 and  $250 \text{ GPa } \mu\text{m}^2$  (numerical results are for  $h_{\text{max}}/R = 0.12$ , experimental data for  $h_{\text{res}}/R \approx 0.11 \pm 0.01$ ). Note the qualitative similarity of the numerical results to Fig. 4b (for  $f_s = 0.995$ ).

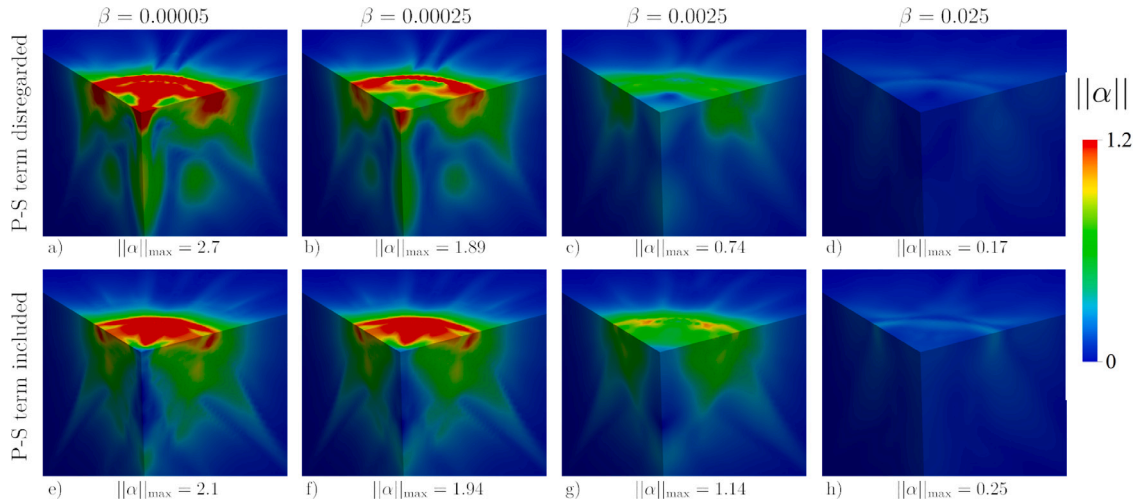


Fig. 14. Distribution of the GND density  $\|\alpha\|$  in the vicinity of the indenter for selected values of parameter  $\beta$  (in GPa $\mu\text{m}^2$ ) for the model without (top row) and with (bottom row) the PS term (for  $h_{\text{max}}/R = 0.12$ , loaded state).

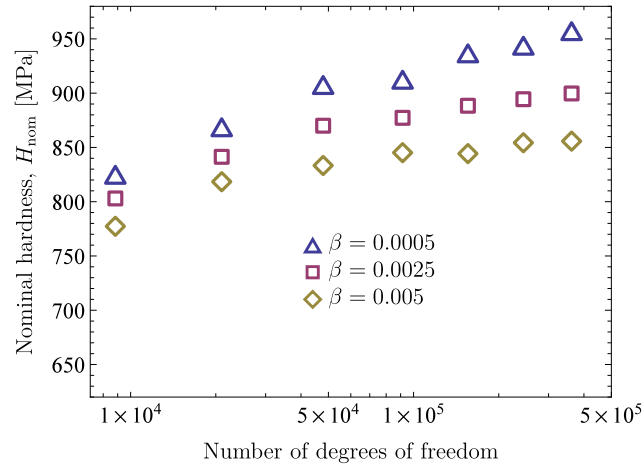


Fig. 15. Dependence of the nominal hardness on the total number of degrees of freedom for a uniformly refined finite-element mesh ( $R = 1.75 \mu\text{m}$ ,  $h_{\text{max}}/R = 0.12$ ).

attempted due to an excessive computational cost). When  $\beta$  is further reduced to  $\beta = 0.0005$  GPa $\mu\text{m}^2$ , a significantly finer mesh would be needed to achieve convergence. Clearly, the effect of  $\beta$  on the hardness itself is consistent with that shown in Fig. 13.

## 7. Conclusion

During non-uniform deformation of an elastic–plastic crystal, spatial incompatibility of the plastic part of the deformation manifests itself in two different ways, through incompatibility of the *accumulated* plastic deformation as well as through incompatibility of the current plastic deformation *rate*. In this paper, the two effects have been combined in a novel way, in terms of  $\kappa$  as the gradient of accumulated rotation  $\phi$  of the crystallographic lattice, and its rate  $\dot{\kappa}$  as the gradient of the lattice spin  $\dot{\phi}$ . Taken separately, the former way represents a specification of the Cosserat crystal plasticity, while the latter represents a specification of the ‘minimal’ gradient enhancement of crystal plasticity proposed by Petryk and Stupkiewicz (2016). To the authors’ knowledge, this combination of two different constitutive descriptions of the gradient effects in plasticity is new and has never been used previously in the calculations of single crystals reported in the literature. In particular, in the present work, the lattice spin gradient  $\kappa$  is introduced for the first time to the PS term in the hardening law (32) proposed by Petryk and Stupkiewicz (2016). It brings a clear computational advantage of using only three components of an increment of  $\phi$  as additional global variables, while accounting for the double-way influence of plastic flow incompatibility on dislocation density measures and related hardening of the crystal.

As shown in the theoretical part of the paper, Sections 2 and 3, the effects of  $\kappa$  and  $\dot{\kappa}$  on the additional crystal hardening caused by plastic flow incompatibility enter into the constitutive description in a different way. The divergence of  $\kappa$  is linearly related to the

back stress  $X_\alpha$ , cf. Eqs. (7) and (11)<sub>2</sub>, and describes kinematic hardening of the crystal since the back stress returns to zero together with  $\kappa$ . In turn, the sign of  $\dot{\kappa}$  does not influence the scalar dislocation density rate  $(\dot{\rho})_G$ , cf. Eqs. (28) and (33)<sub>1</sub>, so that  $\dot{\kappa}$  describes additional isotropic hardening superimposed through Eq. (32) on the conventional anisotropic hardening of the crystal. The two effects are complementary to each other, and their relative significance depends on the values of material parameters which affect the respective internal length scales. This has been demonstrated in detail by the results of calculations of the 1D and 3D examples presented above.

However, there is a substantial difference between the predictive power of the two constitutive ingredients with regard to size effects. While the internal length scale in the Cosserat model is undetermined and can be adjusted by adopting freely the value of parameter  $\beta$ , this is not so in the gradient-enhanced hardening law (32). The natural length scale  $\ell$  in the PS term, of physical meaning through its relation to the dislocation mean free path, is fully determined through standard quantities of a conventional hardening law, so that size effects can be predicted by using the PS term alone. To this end, the parameter  $\beta$  can be taken small enough to reduce the role of the Cosserat part of the model to a needed regularization tool for numerical treatment of the ‘minimal’ gradient enhancement of the classical crystal plasticity, originally implemented in FE framework by Stupkiewicz and Petryk (2016).

This has been done in Section 6, where the numerical predictions of hardness in the spherical indentation test with different indenter radii have been compared to experimental data for a high-purity Cu single crystal. The material parameters were calibrated beforehand to describe the actual material behaviour when the gradient effects are absent or negligible, but then the calculated effect of the indenter radius on hardness was almost exclusively due to the PS term. The obtained agreement with experiment can be regarded as highly satisfactory in view of no adjustment of the internal length scale in a rather simple model. This validates the theoretical approach through the ‘minimal’ gradient extension of conventional crystal plasticity proposed by Petryk and Stupkiewicz (2016) in order to understand the size effect on nominal hardness in the micron scale considered. It has also provided a verification of the regularization technique through the Cosserat model as a computationally more efficient alternative to the implicit-gradient regularization used by Stupkiewicz and Petryk (2016) which led to quantitatively comparable results.

In conclusion, the proposed inclusion of the gradients of both lattice spin,  $\dot{\kappa} = \text{grad } \dot{\phi}$ , and cumulative rotation,  $\kappa = \text{grad } \phi$ , in one constitutive description of a single crystal hardening has proven effective and can be further considered as a promising approach for studying other size effects in plasticity of single crystals and polycrystals.

#### CRediT authorship contribution statement

**M. Rys:** Conceptualization, Methodology, Software, Visualization, Writing – original draft. **S. Stupkiewicz:** Methodology, Writing – original draft, Writing – review & editing. **H. Petryk:** Conceptualization, Methodology, Writing – original draft, Writing – review & editing.

#### Declaration of competing interest

The authors declare that they have no known competing financial interests or personal relationships that could have appeared to influence the work reported in this paper.

#### Acknowledgements

The authors thank Prof. Stanisław Kucharski for providing the raw experimental data of the results published in Kucharski and Woźniacka (2019) and for the related helpful discussions. SS acknowledges the financial support from the National Science Centre (NCN) in Poland through Grant No. 2018/29/B/ST8/00729.

#### Appendix. Computational treatment of the model

Finite-element treatment of the model is based on the weak form of the equilibrium equations (3) that is obtained in a standard manner by multiplying Eq. (3)<sub>1</sub> by the virtual displacement  $\delta u$  and Eq. (3)<sub>2</sub> by the virtual micro-rotation  $\delta \phi$ . Taking the integral of the sum of the two contributions over the body domain  $\Omega$  and integrating by parts yields

$$\int_{\Omega} (\sigma : \delta e + m : \delta \kappa) dV - \int_{\Gamma_t} t \cdot \delta u dS - \int_{\Gamma_M} \mathbf{M} \cdot \delta \phi dS = 0 \quad \forall \delta u, \delta \phi, \quad (\text{A.1})$$

where  $\delta e = \text{grad } \delta u + \epsilon \cdot \delta \phi$  and  $\delta \kappa = \text{grad } \delta \phi$ . The two surface integrals in Eq. (A.1) correspond to the boundary conditions specified by Eq. (4), where  $\Gamma_t$  and  $\Gamma_M$  are the respective parts of the boundary  $\partial\Omega$  ( $\Gamma_t$  and  $\Gamma_M$  may overlap; moreover,  $\delta u$  vanishes on  $\partial\Omega \setminus \Gamma_t$  and  $\delta \phi$  vanishes on  $\partial\Omega \setminus \Gamma_M$ ). Discrete finite-element equations are then obtained by introducing a standard finite-element approximation of the displacement field  $u$  and micro-rotation field  $\phi$ ; the specific choices adopted in this work are commented in Section 4.1.

The time-discrete incremental constitutive equations are obtained by applying the implicit backward-Euler scheme to the rate equations specified in Sections 2 and 3. In the incremental problem at the current time  $t_{n+1} = t_n + \Delta t$ , known are the current displacement gradient  $\mathbf{H}_{n+1}$ , micro-rotation  $\phi_{n+1}$  and its gradient  $\kappa_{n+1}$ , as well as all the involved quantities from the previous time  $t_n$ . The current stress tensor  $\sigma_{n+1}$  and couple-stress tensor  $m_{n+1}$  are given by Eq. (7), where

$$e_{n+1}^e = e_{n+1} - \mathbf{H}_{n+1}^p, \quad \mathbf{H}_{n+1}^p = \mathbf{H}_n^p + \sum_{\alpha} \Delta \gamma_{\alpha} \mathbf{N}_{\alpha}. \quad (\text{A.2})$$

In the adopted computational scheme, which is based on that developed by Stupkiewicz and Petryk (2016), here adjusted to the small-strain setting and Cosserat framework, the local unknowns at each material point (i.e., at each Gauss point in the finite-element setting) comprise the slip increments  $\Delta\gamma_\alpha$  and the current isotropic flow stress  $\tau_{n+1}^c$  that are governed by the following incremental equations,

$$\begin{cases} 0 = \Delta\gamma_\alpha - \Delta t \dot{\gamma}_0 \operatorname{sign}(\tau_{\alpha,n+1}) \left( \frac{|\tau_{\alpha,n+1}|}{\tau_{\alpha,n+1}^c} \right)^m, & \alpha = 1, 2, \dots, \\ 0 = \tau_{n+1}^c - \tau_n^c - \theta_{n+1} (\Delta\gamma + \ell_{n+1} \Delta\chi), \end{cases} \quad (\text{A.3})$$

cf. the respective rate equations (31) and (34). The remaining quantities involved in the description are given by explicit formulae, viz.

$$\begin{aligned} \Delta\gamma &= \sum_\alpha |\Delta\gamma_\alpha|, \\ \Delta\chi &= \sqrt{\Delta\kappa : \Delta\kappa + (\operatorname{tr} \Delta\kappa)^2}, \\ \theta_{n+1} &= \left( 1 - \tau_{n+1}^c / \tau_{\max} \right)^p, \\ \ell_{n+1} &= a^2 \mu^2 b / (2\tau_{n+1}^c \theta_{n+1}), \\ \tau_{\alpha,n+1}^c &= \tau_{\alpha,n}^c + \theta_{n+1} \sum_\beta q_{\alpha\beta} |\Delta\gamma_\beta| + \theta_{n+1} \ell_{n+1} \Delta\chi. \end{aligned} \quad (\text{A.4})$$

The set of nonlinear equations (A.3) is then solved with respect to the local unknowns ( $\Delta\gamma_\alpha, \tau_{n+1}^c$ ) using the Newton method (for an FCC crystal in 3D, there are 13 unknowns and 13 equations). Linearization of the incremental constitutive equations (to obtain the consistent tangent matrix) has been performed using the automatic differentiation (AD) technique available in *AceGen* (Korelc, 2009; Korelc and Wriggers, 2016).

## References

- Acharya, A., Bassani, J.L., 2000. Lattice incompatibility and a gradient theory of crystal plasticity. *J. Mech. Phys. Solids* 48 (8), 1565–1595.
- Alart, P., Curnier, A., 1991. A mixed formulation for frictional contact problems prone to Newton like solution methods. *Comput. Methods Appl. Mech. Engrg.* 92, 353–375.
- Arsenlis, A., Parks, D.M., 1999. Crystallographic aspects of geometrically-necessary and statistically-stored dislocation density. *Acta Mater.* 47, 1597–1611.
- Ashby, M.F., 1970. The deformation of plastically non-homogeneous materials. *Phil. Mag.* 21, 399–424.
- Aslan, O., Cordero, N.M., Gaubert, A., Forest, S., 2011. Micromorphic approach to single crystal plasticity and damage. *Internat. J. Engrg. Sci.* 49, 1311–1325.
- Bargmann, S., Reddy, B.D., Klusemann, B., 2014. A computational study of a model of single-crystal strain-gradient viscoplasticity with an interactive hardening relation. *Int. J. Sol. Struct.* 51, 2754–2764.
- Bayley, C.J., Brekelmans, W.A.M., Geers, M.G.D., 2006. A comparison of structure induced back stress formulations in strain gradient crystal plasticity. *Int. J. Sol. Struct.* 43, 7268–7286.
- Bayley, C.J., Brekelmans, W.A.M., Geers, M.G.D., 2007. A three-dimensional dislocation field crystal plasticity approach applied to miniaturized structures. *Phil. Mag.* 87, 1361–1378.
- Bittencourt, E., Needleman, A., Gurtin, M.E., Van der Giessen, E., 2003. A comparison of nonlocal continuum and discrete dislocation plasticity predictions. *J. Mech. Phys. Solids* 51, 281–310.
- Bronkhorst, C.A., Kalidindi, S.R., Anand, L., 1992. Polycrystalline plasticity and the evolution of crystallographic texture in FCC metals. *Philos. Trans. R. Soc. Lond. A Math. Phys. Eng. Sci.* 341 (1662), 443–477.
- Cermelli, P., Gurtin, M.E., 2002. Geometrically necessary dislocations in viscoplastic single crystals and bicrystals undergoing small deformations. *Int. J. Sol. Struct.* 39 (26), 6281–6309.
- Chang, H.-J., Gaubert, A., Fivel, M., Berbenni, S., Bouaziz, O., Forest, S., 2012. Analysis of particle induced dislocation structures using three-dimensional dislocation dynamics and strain gradient plasticity. *Comp. Mat. Sci.* 52 (1), 33–39.
- Cheng, J., Lane, R., Kesler, M.S., Brechtel, J., Hu, X., Mirzaeifar, R., Rios, O., Momen, A.M., Nawaz, K., 2021. Experiment and non-local crystal plasticity finite element study of nanoindentation on Al-8Ce-10Mg alloy. *Int. J. Sol. Struct.* 233, 111233.
- Cordero, N.M., Gaubert, A., Forest, S., Busso, E.P., Gallerneau, F., Kruch, S., 2010. Size effects in generalised continuum crystal plasticity for two-phase laminates. *J. Mech. Phys. Solids* 58 (11), 1963–1994.
- Dahlberg, C.F.O., Boåsen, M., 2019. Evolution of the length scale in strain gradient plasticity. *Int. J. Plast.* 112, 220–241.
- De Wit, R., 1981. A view of the relation between the continuum theory of lattice defects and non-Euclidean geometry in the linear approximation. *Internat. J. Engrg. Sci.* 19 (12), 1475–1506.
- Demiral, M., Roy, A., Silberschmidt, V.V., 2013. Indentation studies in bcc crystals with enhanced model of strain-gradient crystal plasticity. *Comp. Mat. Sci.* 79, 896–902.
- Ekh, M., Grymer, M., Runesson, K., Svedberg, T., 2007. Gradient crystal plasticity as part of the computational modelling of polycrystals. *Internat. J. Numer. Methods Engrg.* 72, 197–220.
- Essmann, U., Mughrabi, H., 1979. Annihilation of dislocations during tensile and cyclic deformation and limits of dislocation densities. *Phil. Mag.* 40, 731–756.
- Evers, L.P., Brekelmans, W.A.M., Geers, M.G.D., 2004. Non-local crystal plasticity model with intrinsic SSD and GND effects. *J. Mech. Phys. Solids* 52 (10), 2379–2401.
- Fleck, N.A., Muller, G.M., Ashby, M.F., Hutchinson, J.W., 1994. Strain gradient plasticity: Theory and experiment. *Acta Metall. Mater.* 42, 475–487.
- Forest, S., 2008. Some links between cosserat, strain gradient crystal plasticity and the statistical theory of dislocations. *Phil. Mag.* 88 (30–32), 3549–3563.
- Forest, S., 2009. Micromorphic approach for gradient elasticity, viscoplasticity and damage. *J. Eng. Mech. ASCE* 135, 117–131.
- Forest, S., 2016. Nonlinear regularisation operators as derived from the micromorphic approach to gradient elasticity, viscoplasticity and damage. *Proc. R. Soc. Lond. Ser. A Math. Phys. Eng. Sci.* 472, 20150755.
- Forest, S., Barbe, F., Cailletaud, G., 2000. Cosserat modelling of size effects in the mechanical behaviour of polycrystals and multi-phase materials. *Int. J. Sol. Struct.* 37 (46–47), 7105–7126.
- Forest, S., Cailletaud, G., Sievert, R., 1997. A cosserat theory for elastoviscoplastic single crystals at finite deformation. *Arch. Mech.* 49, 705–736.
- Forest, S., Sedláček, R., 2003. Plastic slip distribution in two-phase laminate microstructures: dislocation-based versus generalized-continuum approaches. *Phil. Mag.* 83 (2), 245–276.
- Gao, H., Huang, Y., Nix, W.D., Hutchinson, J.W., 1999. Mechanism-based strain gradient plasticity—I. Theory. *J. Mech. Phys. Solids* 47, 1239–1263.

- Gao, Y.F., Larson, B.C., Lee, J.H., Nicola, L., Tischler, J.Z., Pharr, G.M., 2015. Lattice rotation patterns and strain gradient effects in face-centered-cubic single crystals under spherical indentation. *J. Appl. Mech.* 82 (6), 061007.
- Gurtin, M.E., 2000. On the plasticity of single crystals: free energy, microforces, plastic-strain gradients. *J. Mech. Phys. Solids* 48, 989–1036.
- Gurtin, M.E., 2008. A finite-deformation, gradient theory of single-crystal plasticity with free energy dependent on densities of geometrically necessary dislocations. *Int. J. Plast.* 24 (4), 702–725.
- Gurtin, M.E., Anand, L., Lele, S.P., 2007. Gradient single-crystal plasticity with free energy dependent on dislocation densities. *J. Mech. Phys. Solids* 55, 1853–1878.
- Han, C.S., Gao, H., Huang, Y., Nix, W.D., 2005. Mechanism-based strain gradient crystal plasticity—I. Theory. *J. Mech. Phys. Solids* 53, 1188–1203.
- Hutchinson, J.W., 1976. Bounds and self-consistent estimates for creep of polycrystalline materials. *Proc. R. Soc. Lond. Ser. A Math. Phys. Eng. Sci.* 348, 101–127.
- Jebahi, M., Cai, L., Abed-Meraim, F., 2020. Strain gradient crystal plasticity model based on generalized non-quadratic defect energy and uncoupled dissipation. *Int. J. Plast.* 126, 102617.
- Kaiser, T., Menzel, A., 2019. A dislocation density tensor-based crystal plasticity framework. *J. Mech. Phys. Solids* 131, 276–302.
- Kocks, U.F., 1970. The relation between polycrystal deformation and single-crystal deformation. *Metall. Trans.* 1 (5), 1121–1143.
- Kocks, U.F., Mecking, H., 2003. Physics and phenomenology of strain hardening: the FCC case. *Prog. Mater. Sci.* 48, 171–273.
- Korelc, J., 2009. Automation of primal and sensitivity analysis of transient coupled problems. *Comput. Mech.* 44, 631–649.
- Korelc, J., Šolinc, U., Wriggers, P., 2010. An improved EAS brick element for finite deformation. *Comput. Mech.* 46 (4), 641–659.
- Korelc, J., Wriggers, P., 2016. *Automation of Finite Element Methods*. Springer.
- Kröner, E., 1958. *Kontinuumstheorie Der Versetzungen Und Eigenspannungen*. Springer.
- Kröner, E., 1963. On the physical reality of torque stresses in continuum mechanics. *Internat. J. Engrg. Sci.* 1 (2), 261–278.
- Kröner, E., 1981. Continuum theory of defects. In: Ballian, R., Klemm, M., Poirer, J.-P. (Eds.), *Physics of Defects*. North-Holland, Amsterdam, pp. 215–315.
- Kucharski, S., Stupkiewicz, S., Petryk, H., 2014. Surface pile-up patterns in indentation testing of Cu single crystals. *Exp. Mech.* 54 (6), 957–969.
- Kucharski, S., Woźniacka, S., 2019. Size effect in single crystal copper examined with spherical indenters. *Metall. Mater. Trans. A* 50 (5), 2139–2154.
- Kuroda, M., Tvergaard, V., 2008. A finite deformation theory of higher-order gradient crystal plasticity. *J. Mech. Phys. Solids* 56, 2573–2584.
- Lee, W.B., Chen, Y.P., 2010. Simulation of micro-indentation hardness of FCC single crystals by mechanism-based strain gradient crystal plasticity. *Int. J. Plast.* 26 (10), 1527–1540.
- Lengiewicz, J., Korelc, J., Stupkiewicz, S., 2011. Automation of finite element formulations for large deformation contact problems. *Internat. J. Numer. Methods Engrg.* 85, 1252–1279.
- Lewandowski, M.J., Stupkiewicz, S., 2018. Size effects in wedge indentation predicted by a gradient-enhanced crystal-plasticity model. *Int. J. Plast.* 109, 54–78.
- Lewandowski-Szewczyk, M.J., Stupkiewicz, S., 2020. Non-standard contact conditions in generalized continua: microblock contact model for a Cosserat body. *Int. J. Sol. Struct.* 202, 881–894.
- Mayeur, J.R., McDowell, D.L., 2011. Bending of single crystal thin films modeled with micropolar crystal plasticity. *Internat. J. Engrg. Sci.* 49 (12), 1357–1366.
- Mayeur, J.R., McDowell, D.L., 2013. An evaluation of higher-order single crystal strength models for constrained thin films subjected to simple shear. *J. Mech. Phys. Solids* 61, 1935–1954.
- Mayeur, J.R., McDowell, D.L., 2014. A comparison of Gurtin type and micropolar theories of generalized single crystal plasticity. *Int. J. Plast.* 57, 29–51.
- Mayeur, J.R., McDowell, D.L., 2015. Micropolar crystal plasticity simulation of particle strengthening. *Modell. Simul. Mater. Sci. Eng.* 23, 065007.
- Mayeur, J.R., McDowell, D.L., Bammann, D.J., 2011. Dislocation-based micropolar single crystal plasticity: Comparison of multi- and single criterion theories. *J. Mech. Phys. Solids* 59, 398–422.
- Menzel, A., Steinmann, P., 2000. On the continuum formulation of higher gradient plasticity for single and polycrystals. *J. Mech. Phys. Solids* 48 (8), 1777–1796.
- Naghdi, P.M., Srinivasa, A.R., 1993. A dynamical theory of structures solids. I basic developments. *Philos. Trans. R. Soc. Lond. A Math. Phys. Eng. Sci.* 345 (1677), 425–458.
- Neff, P., Chelmiński, K., Müller, W., Wiener, C., 2007. A numerical solution method for an infinitesimal elasto-plastic Cosserat model. *Math. Models Methods Appl. Sci.* 17 (08), 1211–1239.
- Nix, W.D., Gao, H., 1998. Indentation size effects in crystalline materials: A law for strain gradient plasticity. *J. Mech. Phys. Solids* 46, 411–425.
- Nye, J.F., 1953. Some geometrical relations in dislocated crystals. *Acta Metall.* 1, 153–162.
- Petryk, H., Stupkiewicz, S., 2016. A minimal gradient-enhancement of the classical continuum theory of crystal plasticity. Part I: The hardening law. *Arch. Mech.* 68, 459–485.
- Petryk, H., Stupkiewicz, S., Kucharski, S., 2017. On direct estimation of hardening exponent in crystal plasticity from the spherical indentation test. *Int. J. Sol. Struct.* 112, 209–221.
- Ryś, M., Forest, S., Petryk, H., 2020. A micromorphic crystal plasticity model with the gradient-enhanced incremental hardening law. *Int. J. Plast.* 128, 102655.
- Ryś, M., Petryk, H., 2018. Gradient crystal plasticity models with a natural length scale in the hardening law. *Int. J. Plast.* 111, 168–187.
- Sauzay, M., Kubin, L.P., 2011. Scaling laws for dislocation microstructures in monotonic and cyclic deformation of fcc metals. *Prog. Mater. Sci.* 56, 725–784.
- Scherer, J.M., Besson, J., Forest, S., Hure, J., Tanguy, B., 2019. Strain gradient crystal plasticity with evolving length scale: Application to voided irradiated materials. *Eur. J. Mech. A Solids* 77, 103768.
- Scherer, J.-M., Phalke, V., Besson, J., Forest, S., Hure, J., Tanguy, B., 2020. Lagrange multiplier based vs micromorphic gradient-enhanced rate-(in) dependent crystal plasticity modelling and simulation. *Comput. Methods Appl. Mech. Engrg.* 372, 113426.
- Schmid, E., Boas, W., 1950. *Plasticity of Crystals*. Hughes, London.
- Sedláček, R., Forest, S., 2000. Non-local plasticity at microscale: A dislocation-based and a cosserat model. *Phys. Status Solidi b* 221 (2), 583–596.
- Shim, S., Bei, H., George, E.P., Pharr, G.M., 2008. A different type of indentation size effect. *Scr. Mater.* 59, 1095–1098.
- Shu, J.Y., Fleck, N.A., Van der Giessen, E., Needleman, A., 2001. Boundary layers in constrained plastic flow: comparison of nonlocal and discrete dislocation plasticity. *J. Mech. Phys. Solids* 49, 1361–1395.
- Simmons, G., Wang, H., 1971. *Single Crystal Elastic Constants and Calculated Aggregate Properties*. M.I.T. Press, Cambridge, MA.
- Steinmann, P., 1996. Views on multiplicative elastoplasticity and the continuum theory of dislocations. *Internat. J. Engrg. Sci.* 34, 1717–1735.
- Stupkiewicz, S., Petryk, H., 2016. A minimal gradient-enhancement of the classical continuum theory of crystal plasticity. Part II: Size effects. *Arch. Mech.* 68, 487–513.
- Taylor, G.I., 1934. The mechanism of plastic deformation of crystals. Part I. Theoretical. *Proc. R. Soc. Lond. Ser. A Math. Phys. Eng. Sci.* 145, 362–387.
- Wulfinghoff, S., Böhlke, T., 2012. Equivalent plastic strain gradient enhancement of single crystal plasticity: theory and numerics. *Proc. R. Soc. Lond. Ser. A Math. Phys. Eng. Sci.* 468, 2682–2703.
- Xiao, X., Chen, L., Yu, L., Duan, H., 2019. Modelling nano-indentation of ion-irradiated FCC single crystals by strain-gradient crystal plasticity theory. *Int. J. Plast.* 116, 216–231.
- Yavari, A., Goriely, A., 2012. Riemann–Cartan geometry of nonlinear dislocation mechanics. *Arch. Ration. Mech. Anal.* 205 (1), 59–118.
- Yefimov, S., Van der Giessen, E., 2005. Multiple slip in a strain-gradient plasticity model motivated by a statistical-mechanics description of dislocations. *Int. J. Sol. Struct.* 42 (11), 3375–3394.